Cronfa - Swansea University Open Access Repository

_____

This is an author produced version of a paper published in :
Metallurgical and Materials Transactions A

_____

Cronfa URL for this paper:

_____

Paper:

_____

Advanced Procedures for Long-Term Creep Data Prediction for 2.25 Chromium Steels

M.T.Whittaker and B. Wilshire

Materials Research Centre, Swansea University, Swansea, SA2 8PP, UK

Abstract

A critical review of recent creep studies concludes that traditional approaches such as steady-state behaviour, power law equations and the view that diffusional creep mechanisms are dominant at low stresses should be seriously reconsidered. Specifically, creep strain rate against time curves show that a decaying primary rate leads into an accelerating tertiary stage, giving a minimum rather than a secondary period. Conventional steady state mechanisms should therefore be abandoned in favour of an understanding of the processes governing strain accumulation and the damage phenomena causing tertiary creep and fracture. Similarly, creep always takes place by dislocation processes, with no change to diffusional creep mechanisms with decreasing stress, negating the concept of deformation mechanism maps. Alternative descriptions are then provided by normalizing the applied stress through the ultimate tensile stress and yield stress at the creep temperature. In this way, the resulting Wilshire equations allow accurate prediction of 100,000h creep data using only property values from tests lasting 5000h for a series of 2.25 chromium steels, namely Grades 22, 23 and 24.

Introduction

For over half a century, many large-scale components and structures in electricity generating plant operating at temperatures up to around 840K (565°C) have been manufactured from Grade 22 (2.25Cr-1Mo) steels, where a dispersion of molybdenum carbide particles provides the high temperature strength, while the chromium confers resistance to oxidation during plant exposure. These materials have been extensively used for superheater and reheater tubing, as well as for headers and piping [1]. As a consequence of this widespread adoption, major sets of creep data are available [1], with information systematically gathered by the National Institute of Materials Science (NIMS), Japan, on Gr. 22 steels supplied as

    (a)   quenched and tempered plate for pressure vessels [2],

    (b)   normalized and tempered plate for boiler and pressure vessels [3] and

    (c)   tube for boilers and heat exchangers [4].

In addition, the creep properties have been supplemented by detailed microstructural studies of these as-received and crept bainitic materials [5].

The substantial data sets mean that many engineering design properties are known, such as the stresses which can be applied without causing creep fracture to occur within the planned design life, usually 250,000h. In turn, these estimates are based on the 'allowable tensile creep strengths', determined [6] as 67% of the average

stress (up to 1088K) or 80% of the minimum stress causing rupture in 100,000h (3.6 x 10^8 s) or as the average stress producing a creep rate of 0.01%/1000h (~3 x 10^{-11} s^{-1}). With Grade 22 steels, because tests have been completed for creep lives of 100,000h and more, the allowable creep strengths have been measured accurately. However, with two new 2.25%Cr steels produced with improved creep resistance in order to reduce the wall thicknesses and construction costs of modern plant operating up to about 840K, the maximum creep lives reported in current test programmes are less than 30,000h [7,8]. Consequently, for these two steels, Grade 23 (2.25Cr-1.6W) and Grade 24 (2.25Cr-1Mo-0.3V), valid extrapolation procedures are needed to produce 100,000h creep strengths.

In Europe, tests lasting up to 30,000h have been undertaken for several batches of many steel grades [9]. Unfortunately, using these results, the 100,000h creep strengths depend on the methods chosen to make the calculations, despite the international activities devoted to the assessment of different numerical procedures [10]. Moreover, with a series of 9-12Cr steels introduced to allow plant operating temperatures to be raised to over 870K, the allowable strengths have been reduced progressively as the maximum test duration has increased above 30,000h towards 100,000h and more [11-13]. For this reason, it has been proposed that short-term results should be excluded from the analyses [14,15], but no reliable criteria have been agreed to decide upon the test values which should be discarded.

In contrast to the idea that short-term results should be ignored [14,15], very recently, a new methodology has suggested that the allowable creep strengths can

be computed precisely from measurements under stress/temperature conditions giving creep lives up to 5000h (and, certainly, 30,000h). This new concept, termed the Wilshire equations [16-20], quantifies the dependencies on stress (σ) and temperature (T) of commonly monitored quantities, such as the minimum creep rate ($\dot{\varepsilon}_m$), the time to fracture (t_f) and the times to pre-defined strains (t_ε). Thus, the creep life is presented as

$$\left(\sigma / \sigma_{TS}\right) = \exp\left\{-k_1\left[t_f . \exp\left(-Q_c^* / RT\right)\right]^u\right\} \tag{1}$$

where R=8.314Jmol^{-1}K^{-1}. In this case, Q_c* is the activation energy measured at constant (σ/σ_{TS}), with σ_{TS} being the ultimate tensile strength determined in high-strain-rate (~10^{-3}s^{-1}) tensile tests carried out at the creep temperatures for each batch of material investigated. Similarly, the minimum creep rates are described as

$$\left(\sigma / \sigma_{TS}\right) = \exp\left\{-k_2\left[\dot{\varepsilon}_m . \exp\left(Q_c^* / RT\right)\right]^v\right\} \tag{2}$$

and the times to pre-defined strains are represented as

$$\left(\sigma / \sigma_{TS}\right) = \exp\left\{-k_3\left[t_\varepsilon . \exp\left(-Q_c^* / RT\right)\right]^w\right\} \tag{3}$$

where k_1, k_2 and k_3, as well as u, v and w, can be derived from reasonable property sets obtained over a range of relevant creep temperatures.

The $\dot{\varepsilon}_m$, t_f and t_ε data can also be rationalized [16-19] by normalizing σ through σ_{PS}, where σ_{PS} is the proof stress for each material batch at the creep temperatures. However, σ_{TS} is preferred. This is because σ_{TS} is the highest stress which can be applied at the creep temperature. Hence, eqns (1), (2) and (3) have the obvious advantage that, with the sigmoidal ln $\dot{\varepsilon}_m$, ln t_f and ln t_ε against (σ/σ_{TS}) plots, $\dot{\varepsilon}_m \rightarrow \infty$, $t_\varepsilon \rightarrow 0$ and $t_f \rightarrow 0$ when $(\sigma/\sigma_{TS}) \rightarrow 1$, while $\dot{\varepsilon}_m \rightarrow 0$, $t_\varepsilon \rightarrow \infty$ and $t_f \rightarrow \infty$ as $(\sigma/\sigma_{TS}) \rightarrow 0$. In any case, on plotting (σ/σ_{TS}) against $\dot{\varepsilon}_m$, t_f or t_ε, it is a straightforward matter to show whether σ is greater or less than σ_{PS}. Then, by applying eqns (1), (2) and (3) to results from tests with maximum creep lives of only 5000h, accurate estimates have been determined for the 100,000h strengths of ferritic [17], bainitic [18] and martensitic steels [19].

For these reasons, the predictive capabilities of eqn (1) are now reviewed for Grade 22 steels in all three heat treated states [2-4], before assessing the allowable tensile stresses calculated for Grades 23 and 24 using the NIMS data for creep lives up to only 5000h [7,8]. Yet, confidence in any extrapolation procedure is enhanced when the methods are based on a sound physical understanding of the mechanisms controlling creep and creep fracture. Hence, the results achieved using the Wilshire equations [16-20] are discussed in relation to the processes shown to control creep strain accumulation and the damage phenomena causing failure of these bainitic 2.25Cr steels.

2.25Cr Materials

All Grade 22 samples were well within the composition limits (wt%) for these materials, namely, 0.05-0.15 C (max), 0.3-0.6 Mn, 0.025 P (max), 0.025 S (max), 0.5 Si, 1.9-2.6 Cr, 0.87-1.3 Mo. The three heat treatments then chosen were

   (a)   1203K for 6h before water quenching and tempering firstly for 6h at 908K then air cooling and secondly 2h at 873K before furnace cooling of the quenched/tempered plate [2],

   (b)   1203K for 1h and air cooled, 1013K for 2h then air cooled and 973K for 4h before furnace cooling of the normalized/tempered plate [3], and

   (c)   1203K for 20 mins, then air cooled to 993K for 130 mins before air cooling of the tube [4].

The composition ranges (wt%) for the tube and pipe specimens of the Grade 23 steels were 0.04-0.10 C, 0.10-0.6 Mn, 0.30 P, 0.01 S, 0.5 Si, 1.9-2.6 Cr, 0.05-0.3 Mo, 1.45-1.75 W. The tube product (designated by NIMS as MnA) was heat treated after hot rolling at 1323K for 10 mins before air cooling, then at 1043K for 60 mins and air cooling. The pipe sample (NIMS designation MnQ) was similarly heat treated at 1323K for 30 mins before air cooling and then 1043K for 60 mins and air cooling [7].

The Grade 24 steel was within the limits <0.17 C, 0.3-0.6 Mn, <0.015 P, <0.01 S, <0.1 Si, 2-2.5 Cr, 0.9-1.1 Mo, 0.25-0.35 V. The sample (NIMS designation VdA), which was not stress relieved after forging, was given 7h at 1293K then water quenched, before

968K for 1h and air cooling. Another Gr.24 sample (NIMS designation VdB) was stress relieved by giving 898K for 10h and air cooling, followed by 978K for 30h and air cooling after the above heat treatment [8].

For the Grade 22 (2.25Cr-1Mo) materials, the heat-treatment schedules produced ferrite-bainite microstructures with around 80% ferrite regions in the tube and almost exclusively bainitic microstructures with both the quenched/tempered and normalized/tempered plates [5]. Again, for the Grade 23 (2.25Cr-1.6W) and the Grade 24 (2.25Cr-1Mo-0.3V) products, fully bainitic structures were produced.

Traditional Approaches to Creep and Creep Fracture

Creep rupture tests were carried out by NIMS for all three of these 2.25Cr steels, recording the creep lives (t_f), the total strains to failure (ε_f) and the reductions in area at fracture (RoA) over ranges of stress and temperature [2,3,4]. The test conditions were such that rupture times in excess of 100,000h at 723 to 923K (450 to 650°C) were measured for the Gr.22 steels in all three heat treated conditions, whereas rupture times approaching only 20,000 to 30,000h at 773 to 923K (500 to 650°C) were monitored for the Gr.23 and Gr.24 products [7,8]. In contrast, while no minimum creep rate values were found for the Gr.24 steels, $\dot{\varepsilon}_m$ measurements have been reported over these temperature ranges for the Gr.22 and Gr.23 samples [2,3,4,21].

In line with common practice developed over half a century and more ago, the minimum creep rates and rupture lives for all three 2.25Cr steels (Gr.22, 23 and 24), irrespective of the heat treatment selected, were described [5] using standard power law equations as

$$M/t_f = \dot{\varepsilon}_m = A\sigma^n \exp(-Q_C / RT) \qquad (4)$$

where the parameters, M and A, the stress exponent (n) and the activation energy for creep (Q_c) vary depending on the stress/temperature ranges considered. With eqn. (4), Q_c is determined from the temperature dependencies of $\dot{\varepsilon}_m$ or t_f at constant σ rather than at constant (σ/σ_{TS}) as in the calculations of Q_c* in eqns (1), (2) and (3).

For all three 2.25Cr steels and every heat treatment, the variations in n and Q_c with eqn. (4) become evident from Figs. 1 to 4 inclusive. Thus, Figs. 1 and 2 reveal the stress and temperature dependencies of $\dot{\varepsilon}_m$ and t_f respectively for the pipe samples of Gr.23 (i.e. P23). Clearly, the stress exponent (n) decreases from around 13 at high stresses at 773K to almost 6 under low stresses at 923K, with the activation energy for creep (Q_c) ranging from about 300 to 535kJmol^{-1} [7]. Similar trends were observed with the log σ/log t_f plots for the other 2.25Cr steels after all heat treatments. For example, Fig.3 illustrates the stress rupture properties at 873K for Gr.22 steel after the three selected heat treatments, indicating that the creep fracture strengths increase in the order of tube and normalized/tempered plate and then quenched/tempered plate in short term tests, while the 100,000h strengths are

comparable. Finally, Fig.4 compares the stress/creep life data for Gr.22, 23 and 24 steels at 873K, suggesting that Gr.23 and 24 are more creep fracture resistant than Gr.22 for creep lives up to 30,000h, so that the wall thicknesses of components and structures can apparently be reduced using these new steels to limit plant construction costs.

Because n and Q_c in eqn. (4) vary in an unpredictable manner, results of the types presented in Figs. 2, 3 and 4 cannot be used to derive long-term stress rupture properties from short-term data. For this reason, the NIMS creep life values for the Gr.22 steels were analysed [5] as functions of the Larson-Miller parameter (P_{LM}), namely,

$$P_{LM} = T_K(20 + \log t_R) \tag{5}$$

where T_K is in Kelvin and t_R in hours [22]. Evidently, from Fig.5, all three heat treatments received by the Gr.22 steel gave similar 100,000h strengths, but with the quenched/tempered product displaying longer creep lives above about 80MPa [5]. In fact, from Fig.5, while the plot for the quenched/tempered material curves continuously, a curvature change is found as the stress falls below around 150MPa for both the Gr.22 tube and normalized/tempered samples. This curvature change means that, for these two heat treatments, extrapolation of results for σ>150MPa underestimate the creep lives observed when σ<150MPa.

For Gr.22 steels after all three heat treatments, the longest creep lives were in excess of 100,000h (see Fig.3), so the 100,000h creep rupture strengths obtained using the Larson-Miller approach would be expected to be accurate. These values for temperatures of 773, 823 and 873K are presented in Table I [5], with similar estimates published by other research groups also using long-term data sets [1]. However, Larson-Miller plots were not produced by NIMS for the Gr.23 and 24 steels [7,8], presumably because, with maximum creep lives less than 30,000h, confidence could not be placed in this parametric Larson-Miller method of data extrapolation.

Rationalization of Power Law Behaviour

Whilst eqns. (1), (2) and (3) have σ normalized through σ_{TS}, eqn (4) makes no such provision. However, it is easy to modify the power law expression to include σ_{TS}, so that eqn. (4) becomes

$$M/t_f = \dot{\varepsilon}_m = A^* \left(\sigma / \sigma_{TS} \right)^n \exp(-Q_c^* / RT) \qquad (6)$$

where $A^* \neq A$ and $Q_c^* \neq Q_c$[16-20].

Adopting eqn. (6), the data sets shown for P23 in Figs. 1 and 2 are superimposed onto single master curves [23] by plotting log $\dot{\varepsilon}_m$ and log t_f as functions of log(σ/σ_{TS}) rather than log σ, using an activation energy (Q_c^*) of 230kJmol^{-1} (Figs. 6 and 7). Even so, this procedure does not eliminate the decrease from $n \cong 13$ to $n \cong 6$, so that the

unknown curvatures of the plots in Figs. 6 and 7 still do not allow confident prediction of long-term properties by extrapolation of short-term results for the P23 steel.

Behaviour patterns similar to those shown in Figs. 6 and 7 for the P23 product [23] were also found when eqn.(6) was used to quantify the stress rupture values for the Gr.22 steels in all three heat treated conditions [24]. For example, with the Gr.22 tube, the individual log σ/log t_f lives at different temperatures obtained using eqn. (4) (Fig.8) are superimposed by choosing eqn (6), with a Q_c^* value of 280kJmol^{-1} (Fig.9). Once again, this superimposition does not alter the decrease from $n \cong 14$ to $n \cong 3.5$ with decreasing stress and increasing temperature, so the unknown curvatures of these plots again prevent extended extrapolation.

In the original studies [23,24], the activation energies of 230kJmol^{-1} for the P23 samples and 280kJmol^{-1} for the three Gr.22 materials were thought to coincide with the activation energy for lattice self diffusion in the bainitic matrices. However, it would seem surprising if the replacement of the 1%Mo in Gr.22 steels by 1.6%W in the P23 specimens changed the matrix self diffusion values by this amount. Alternatively, this difference in Q_c^* may be a consequence of differences in the test conditions selected for these materials, expecting that the activation energy changes as the stress/temperature ranges were altered. Thus, temperatures of 723 to 923K were chosen for the Gr.22 products compared with 773 to 923K with the P23. Moreover, with the quenched/tempered Gr.22 specimens, tests were always carried out with $\sigma < \sigma_{PS}$, whereas the tests with the tube and normalized/tempered Gr.22

steels were undertaken at stresses above and below σ_{PS}. Hence, it is necessary to clarify whether variations in test conditions can cause changes in the values of Q_c*.

Creep Data Analysis for Grade 22 Steels

By normalizing σ through σ_{TS}, the value of Q_c* should be the same, irrespective of whether the data rationalization is performed using eqns. (1), (2) and (3) or eqn. (6). Hence, the variations in Q_c* for the Gr.22 steels in all three heat-treated conditions are now addressed by using eqn. (2) to define the $\dot{\varepsilon}_m$ measurements as functions of stress and temperature.

Adopting eqn. (2), the values of k_2, v and Q_c* have been determined [24] by plotting $\ln[\dot{\varepsilon}_m \exp(Q_c*/RT)]$ against $\ln[-\ln(\sigma/\sigma_{TS})]$, with different behaviour patterns observed for the three heat treatments.

(a)   For the quenched/tempered plate, the plot in Fig.10 is essentially a single straight line, with k_2= 16.5, v= -0.157 and Q_c*=230kJmol^{-1} for stresses such that σ is less than $0.65\sigma_{PS}$ (<$0.4\sigma_{TS}$).

(b)   For the normalized/tempered plate, a single straight line relationship is also found between $\ln[\dot{\varepsilon}_m \exp(Q_c*/RT)]$ against $\ln[-\ln(\sigma/\sigma_{TS})]$ for test temperatures of 748-823K, but a high degree of scatter in the $\dot{\varepsilon}_m$ results for 723K meant that these low temperature results were not analyzed. Even so, for the high temperature measurements, the behaviour patterns in Fig.11 are similar to those for the quenched/tempered product in Fig.10. Thus, k_2 = 12.4 and v = -

0.131. Moreover, for this straight line segment, the value of Q_c^* was calculated to minimize the least squares fitting error which superimposed the data in Fig.11 onto the best straight line. This procedure again gave Q_c^*=230kJmol^{-1} when $\sigma<0.4\sigma_{TS}<0.65\sigma_{PS}$.

(c)   For the Gr.22 tube, using eqn.(2) with Q_c^*=280kJmol^{-1}, the $\ln[\dot{\varepsilon}_m \exp(Q_c^*/RT)]$ against $\ln[-\ln(\sigma/\sigma_{TS})]$ plot in Fig.12 showed three distinct straight line regions. For each straight line section, Q_c^* was then determined as the value which minimized the least squares fitting error to superimpose the individual points onto the best straight line. The results for each straight line segment were then reanalyzed to calculate the best values of k_2 and v for the appropriate Q_c^* value. With this procedure, changes in Q_c^* occur such that Q_c^*=280kJmol^{-1} for $\sigma>0.4\sigma_{TS}$ ($\cong 0.65\sigma_{PS}$), Q_c^*=230kJmol^{-1} for $0.4\sigma_{TS}>\sigma>0.2\sigma_{TS}$, whereas Q_c^* rises again to around 280kJmol^{-1} when σ falls from above to below $0.2\sigma_{TS}$. Thus, the creep rates when $0.4\sigma_{TS}>\sigma >0.2\sigma_{TS}$ are slower than those which would be anticipated by extrapolation of $\dot{\varepsilon}_m$ values when $\sigma>0.4\sigma_{TS}$, while the $\dot{\varepsilon}_m$ measurements when $\sigma<0.2\sigma_{TS}$ are very much faster than those expected by direct extrapolation of results when $0.4\sigma_{TS}>\sigma >0.2\sigma_{TS}$.

Over the stress/temperature ranges over which straight line segments are shown in Figs. 10, 11 and 12, the best values of k_2, v and Q_c^* for the Gr.22 steels in the three heat-treated states are included in Table II. These figures were obtained by using all available data for the Gr.22 steels, although the results were very similar when only the $\dot{\varepsilon}_m$ measurements for $t_f<5000$h were taken. Inserting the values of k_2, v and Q_c^*

into eqn. (2) then accurately describes the log σ/log $\dot{\varepsilon}_m$ plots for the Gr.22 steels, as illustrated by the complex behaviour of the tube material in Fig. 13.

Creep Life Prediction for Grade 22 Steels

Because eqn. (2) accurately describes the log σ/log $\dot{\varepsilon}_m$ data, for example in Fig. 13, it is relevant to consider the manner in which eqn. (1) quantifies the stress rupture properties of the Gr.22 steels. In this way, an assessment can be made of the precision with which the 100,000h creep rupture strengths calculated using eqn. (1) with t_f values of no more than 5000h predicts the allowable strengths of these steels determined by applying the Larson-Miller method to long-term data (Table I).

Using eqn. (1), plotting $\ln[t_f.\exp(-Q_c^*/RT)]$ against $\ln[-\ln(\sigma/\sigma_{TS})]$ emphasises that behaviour patterns are found (Figs. 14, 15 and 16) which are comparable to those previously recorded by adopting eqn. (2) to describe the creep rate properties of the Gr.22 steels in all three heat treated conditions (Figs. 10, 11 and 12). Essentially,

(a)   a single straight line represents the stress rupture properties of the quenched/tempered plate (Fig. 14),

(b)   with far lower scatter levels in the t_f data than in the $\dot{\varepsilon}_m$ results [3], using eqn.(1) with Q_c^*=280kJmol^{-1}, two intersecting straight line segments were revealed using all of the stress rupture measurements for the normalized/tempered Gr.22 plate (Fig.15). This contrasts with to the single line

found when eqn.(2) was used to describe the high-temperature $\dot{\varepsilon}_m$ results (Fig.11), and

(c)   three intersecting straight line segments are recorded using eqn.(1) with $Q_c*=280kJmol^{-1}$ with the Gr.22 tube. (Fig. 16).

Using this information, the best value of Q_c* was determined, with the best values of k_1 and u then recalculated for each straight line segment in Figs.14, 15 and 16. Thus, adopting the procedures described to analyse the $\dot{\varepsilon}_m$ data sets with eqn.(2), the best values of k_1, u and Q_c* for each (σ/σ_{TS}) regime are revealed in Table II using all available stress rupture data. Even so, once again, almost identical results were achieved using only the creep lives for $t_f<5000h$.

While the t_f measurements for the quenched/tempered plate were made largely for $\sigma<\sigma_{PS}$, with the Gr.22 tube and normalized/tempered plate, the creep lives recorded when $\sigma<0.4\sigma_{TS}$ are longer than expected by extrapolation of data reported when $\sigma>0.4\sigma_{TS}$. However, with the Gr.22 tube, the creep lives become distinctly shorter when $\sigma<0.2\sigma_{TS}$ than the estimates anticipated by extrapolation of measurements when $0.4\sigma_{TS}>\sigma>0.2\sigma_{TS}$. In addition, as found for the minimum creep rates (Figs. 10, 11 and 12), $Q_c*\cong 280kJmol^{-1}$ when $\sigma>0.4\sigma_{TS}$, while $Q_c*\cong 230kJmol^{-1}$ when $0.4\sigma_{TS}>\sigma>0.2\sigma_{TS}$, but with Q_c* rising again towards $280kJmol^{-1}$ when $\sigma<0.2\sigma_{TS}$. On this basis, using the figures in Table II with eqn. (1) provides a very reasonable description of the complex log σ/log t_f behaviour of the Gr.22 tube (Fig. 8) and normalized/tempered plate (Fig. 17).

Inserting the k_1, u and Q_c^* values for each (σ/σ_{TS}) region in Table II into eqn. (1) predicts the 100,000h creep rupture strengths listed for 773, 823 and 873K in Table I. Clearly these figures are close to the estimates obtained by applying the Larson-Miller method to long-term data for 2.25Cr-1Mo steels (Table I). Thus, by adopting the Wilshire equations, 100,000h strengths can be predicted accurately by consideration of reasonable sets of t_f measurements carried out over appropriate temperature ranges under test conditions giving creep lives less than 5000h. However, it then becomes necessary to explain, in mechanistic terms, the reasons for the variations in k_1, u and Q_c^* (eqn.(1)) and in k_2, v and Q_c^* (eqn.(2)), shown in Table II.

Alternative Interpretations of Creep Behaviour

When using power law equations, eqns.(4) and (6), the normal tensile creep curves showing the increase in creep strain (ε) with time (t) in Fig.18 are widely considered to consist of three distinct stages. Following the initial strain on loading (ε_0), the creep rate ($\dot{\varepsilon} = d\varepsilon/dt$) decreases during the primary stage, reaching a minimum or secondary rate ($\dot{\varepsilon}_m$) before accelerating once again during the tertiary stage which terminates in fracture. In terms of the processes governing the creep strain rate, in general, the primary and tertiary stages have then been ignored to focus on the mechanisms controlling secondary or steady state behaviour [25].

Considering steady state creep of pure metals, it is commonly believed that dislocation processes are rate controlling when $n \cong 4$ or more [25,26], with diffusional creep mechanisms not involving dislocation movement being dominant when $n \cong 1$ [25,26]. This view has led to the concept of deformation mechanism maps where the creep processes are identified with specific σ/T regimes on graphs plotting σ/E, where E is Youngs modulus, against T/T_m, where T_m is the absolute melting point [25,26]. Yet, while various dislocation processes have been proposed to explain $n \cong 4$ behaviour of pure metals [27], no one theory is fully compatible with all of the experimental facts [28]. It must also be recognized that no acceptable explanation has been advanced [29] to account for the observation that n>>4 at high stresses with particle-hardened alloys (as illustrated in Figs.1 to 4 inclusive). Moreover, very recently, a critical assessment of the evidence commonly quoted in support of diffusional creep mechanisms determining the properties displayed when $n \cong 1$ has revealed that dislocation processes are dominant, irrespective of the n value recorded for both pure metals and particle-hardened alloys [30].

The evidence negating diffusional creep mechanisms in favour of dislocation creep processes [30] can be summarized as follows.

(a)   With pure copper, when the simple sigmoidal ln $\dot{\varepsilon}_m/(\sigma/\sigma_{TS})$ curve in Fig.19 obtained with eqn.(2) is replotted as a power law (eqn.(6)) in Fig.20, the results predict not only the decrease from $n \cong 4$ to $n \cong 1$ at low stresses but also the power law 'breakdown' region when n>>4 at high stresses [16]. Thus, there is no justification for assuming that different creep mechanisms become dominant in the $n \cong 1$, $n \cong 4$ and n>>4 regimes.

(b)   Although dislocation mechanisms are always dominant at all stress levels, with

polycrystalline copper, a transition in the detailed dislocation processes

governing creep deformation take place when σ falls from above to below σ_Y,

where σ_Y is the yield stress at the creep temperature [16]. Thus, when $\sigma < \sigma_Y$,

the initial specimen strain on loading (ε_0) increases elastically with increasing

stress, whereas ε_0 increases more rapidly when ε_0 has a larger plastic

component for $\sigma > \sigma_Y$ (Fig.21). On this basis, dislocations multiply rapidly

within the grains during the initial plastic strain when $\sigma > \sigma_Y$, while creep must

occur not by the generation of new dislocations but by the movement of

dislocations pre-existing in the as-received microstructure when $\sigma < \sigma_Y$. In the

low stress regime, deformation by dislocation generation within the grains is

inhibited, so that creep occurs only in the grain boundary zones, where zone

deformation comprises grain boundary sliding and associated dislocation

movement in grain regions adjacent to the boundaries [31]. In this way, the

creep rates become progressively slower and the creep lives longer when

$\sigma < \sigma_Y$, compared with the values anticipated by linear extrapolation of data

collected when $\sigma > \sigma_Y$.

(c)   With alloys strengthened by fine dispersions of precipitates or insoluble

particles, the observation that precipitate-free zones (PFZs) can form on

boundaries normal to the applied tensile stress has been widely attributed to

the occurrence of diffusional creep mechanisms [32,33]. However, these PFZs

can be present and increase in width when n>>1 [34]. Moreover, for a range of

two-phase alloys, it has been shown [20] that PFZs are found only when they

are developed initially in the thermo-mechanical processing treatments prior

to creep exposure (Fig.22a). These microstructural features cannot therefore be formed by diffusional creep processes but can increase in width as dislocation activity concentrates in these boundary zones under low applied stresses (Fig.22b).

As with the assumed transition from dislocation to diffusional creep mechanisms represented by deformation mechanism maps [25,26], the emphasis currently placed on interpretation of 'steady state' creep behaviour has also been seriously questioned [16,30]. Thus, in Fig.23, the variations in creep strain rate ($\dot{\varepsilon}$) with time are shown for 2.25Cr-1Mo steel, proving that the decaying primary rate gives way to an accelerating tertiary stage. With very few exceptions [16,30], such as superpurity aluminium at temperatures around $0.5T_m$ [27] and single crystals in the absence of recrystallization during creep [16], a minimum rather than a secondary or steady state creep rate is therefore recorded. In addition, the shapes of the creep curves depend on the stress/temperature conditions imposed, most frequently with the primary stage becoming less pronounced and the tertiary stage more dominant with decreasing stress and increasing temperature. On this basis, rather than focussing on steady state properties, tensile creep behaviour patterns should be discussed in relation to the dislocation processes controlling creep strain accumulation and the damage phenomena causing the tertiary acceleration and eventual failure.

Creep Deformation Processes for Grade 22 Steels

As previously found for 1Cr-0.5Mo ferritic steel [17], behaviour patterns similar to those observed for copper tested above and below σ_Y (Fig.21) are recorded for the present 2.25Cr-1Mo tube steel. As evident from Fig.24, ε_0 increases elastically with increasing stress until $\sigma=0.65\sigma_{PS}$, but then increases more rapidly with a larger plastic component of ε_0 when $\sigma > 0.65\sigma_{PS}$, seemingly with $\sigma_Y \cong 0.65\sigma_{PS}$. It is then a straightforward matter to rationalize the property trends when eqn. (2) is applied to the creep data for the Gr.22 steels given the three different heat treatments (Figs. 10,11 and 12).

(a)   With the quenched/tempered plate, there is no break in the $\ln[t_f \exp(-Q_c^*/RT)]$ against $\ln[-\ln(\sigma/\sigma_{TS})]$ plot (Fig.10) because all tests were carried out at stresses less than $0.65\sigma_{PS}$ ($\cong \sigma_Y$). Hence, deformation is always confined to the grain boundary zones.

(b)   With the tube and normalized/tempered products, a break in the $\ln[t_f \exp(-Q_c^*/RT)]$ against $\ln[-\ln(\sigma/\sigma_{TS})]$ plot again occurs at $\sigma \cong 0.4\sigma_{TS} \cong 0.65\sigma_{PS} \cong \sigma_Y$ (Figs. 11 and 12). In line with the Larson-Miller plots for these steels in Fig.5, the creep lives therefore become longer than expected by direct extrapolation of results when $\sigma > \sigma_Y$, because grain deformation is restricted so that creep occurs only by grain boundary zone deformation when $\sigma < \sigma_Y$.

(c)   With the tube material, a second break occurs in Fig.12 when $\sigma \cong 0.2\sigma_{TS} \cong 0.35\sigma_{PS}$. This is a consequence of the bainite regions in the initial ferrite/bainite microstructure degrading to ferrite and molybdenum carbide particles in long-term tests, with very coarse carbides along grain boundaries.

As a result, the creep rates are faster and the creep lives are significantly shorter in tests of long duration at 873K and above than would be expected by extrapolation of the property sets recorded for $0.65\sigma_{PS} > \sigma > 0.35\sigma_{PS}$ when the bainitic microstructures are present (Fig.12).

For all three heat treatments carried out for the Gr.22 steels, the gradual loss of creep strength with increasing test duration at higher creep temperatures is attributable to the progressive coarsening of the molybdenum carbide particles [5]. However, it is only with the Gr.22 tube product that further property changes occur with the bainite→ferrite transformation in long term tests at high temperatures when σ falls below $0.2\sigma_{TS}$ ($\cong 0.35\sigma_{PS}$).

This interpretation of the creep behaviour of the Gr.22 steels is also consistent with the changes in $Q_c{}^*$ (Table II). Thus, when $\sigma>\sigma_Y$, new dislocations are created during the initial specimen extension, with creep occurring largely as a result of these dislocations moving within the grains. Under these circumstances, $Q_c{}^* \cong 280\text{kJmol}^{-1}$, equivalent to that for self diffusion in bainitic matrices. When $\sigma<\sigma_Y$, so that creep takes place within the grain boundary zones rather than in the grains, $Q_c{}^* \cong 230\text{kJmol}^{-1}$, representing diffusion along dislocations and grain boundaries. However, with the marked loss of creep strength in the Gr.22 tube when $\sigma<0.2\sigma_{TS}$, $Q_c{}^* \cong 280\text{kJmol}^{-1}$, suggesting that diffusion occurs largely within the grains as the creep resistance falls when the bainitic regions transform to ferrite and coarse molybdenum carbide particles in long-term tests at high temperatures.

Creep Fracture Processes in Gr.22 Steels

Although the detailed dislocation processes controlling creep strain accumulation depend on the microstructural changes and test conditions, distinct differences in the creep fracture characteristics are found with the tube and normalized/tempered plate and with the quenched/tempered material. These differences in creep rupture processes can be inferred from plots of the reduction in area at fracture (RoA) and the total elongation at fracture (ε_f) as functions of $\log[t_f \exp(-Q_c^*/RT)]$ in Figs 25, 26 and 27.

For all test conditions covered for the tube [4] and normalized/tempered plate [3], the RoA values are usually in excess of 0.8, while the majority of the ε_f data were in the range 0.2 to 0.6 (Figs.25 and 26). So, with RoA> ε_f, failure was preceded by extensive necking, with fracture occurring in a transgranular manner [5]. For the quenched/tempered plate, similar results were obtained at 723 and 923K, whereas very low values of ε_f and RoA were observed at selected stresses at 773 to 873K (Fig.27), suggesting that failure takes place in an intergranular manner [2]. Even so, these differences in failure mode do not alter the long-term stress/creep life relationships, which appear to be similar for all three heat treatments chosen for the Grade 22 materials (Fig.3).

Creep Behaviour of Grade 23 Steels

For creep lives approaching 30,000h, $\dot{\varepsilon}_m$ measurements are available for the Grade 23 pipe and tube (P23 and T23), with σ_{TS} and σ_{PS} recorded at 773 to 923K [7,21]. Hence, this information is now used to consider the creep properties of these newly developed products.

The log σ/log $\dot{\varepsilon}_m$ plots for P23 in Fig.1 show that a fall occurs from $n \cong 13$ at high stresses to $n \cong 6$ at low stresses, with Q_c ranging from ~ 300 to 535kJmol^{-1} using eqn.(4). These stress/creep rate plots at each test temperature were then superimposed onto a single curve in Fig.6 using eqn.(6), with $Q_c^* \cong 230$kJmol^{-1}. However, with the Grade 22 materials, Q_c^* has now been found to depend on the test conditions imposed (Table II), so eqn.(2) is therefore adopted to analyse the P23 data.

Once again plots were constructed of $\ln[\dot{\varepsilon}_m \exp (Q_c^*/RT)]$ against $\ln[-\ln(\sigma/\sigma_{TS})]$ taking Q_c^*=230kJmol^{-1}. These are shown as Fig.28 for P23 and Fig.29 for T23. In both cases, three straight line segments were apparent. Repeating the procedures adopted for the Gr.22 tube, each straight-line section was analysed to determine the values of Q_c^* which best superimposed the data sets onto single lines. For P23 and T23, the Q_c^* values obtained were 280kJmol^{-1} above about $0.5\sigma_{TS}$ (~$0.55\sigma_{PS}$), 230 kJmol^{-1} down to around $0.3\sigma_{TS}$, rising again to 280 kJmol^{-1} at stresses below about $0.3\sigma_{TS}$ (~$0.4\sigma_{PS}$).

Using the above Q_c^* values for the relevant straight line segments in Figs.28 and 29, the best-fit values of k_2 and v in eqn.2 were determined. These values are included in Table III. As found earlier with the Gr.22 tube, it is a straightforward matter to interpret these variations in k_2, v and Q_c^* in terms of the processes governing creep strain accumulation, assuming that $0.55\sigma_{PS} \cong \sigma_Y$.

At stresses above σ_Y, when new dislocations are generated during the virtually instantaneous strain on loading (ε_0), creep occurs predominantly by the movement of these new dislocations within the grains, with Q_c^* ($=280$kJmol^{-1}) representing the activation energy for lattice diffusion. For $0.5\sigma_{TS}>\sigma>0.3\sigma_{TS}$ ($0.55\sigma_{PS}>\sigma>0.4\sigma_{PS}$), so that $\sigma<\sigma_Y$, creep takes place by movement of dislocations pre-existing in the as-heat-treated states, giving grain boundary zone deformation. In this intermediate σ/σ_{PS} regime, the creep rate is much slower than the values predicted by linear extrapolation of results acquired for $\sigma>0.5\sigma_{TS}$.

In the low stress range, when $\sigma<0.3\sigma_{TS}$ ($<0.4\sigma_{PS}$), Q_c^* rises once more towards 280kJmol^{-1}, showing that creep is again controlled by lattice self diffusion when the microstructure changes from bainite to ferrite with coarse carbide particles along the grain boundaries. Indeed, it has previously been established that the bainitic microstructure degrades such that the original lath-like structure entirely disappears in these long-term tests at the higher test temperatures [21]. As a result of this microstructure degradation, the creep rates when $\sigma<0.4\sigma_{PS}$ are substantially faster than the values predicted by extrapolation of data obtained when $0.55\sigma_{PS}>\sigma>0.4\sigma_{PS}$.

Creep Life Prediction for Grade 23 Steels

The product, $\dot{\varepsilon}_m t_f$ (=M in eqns.(4) and (6)) is not a constant for the P23 and T23 steels [7]. As shown in Fig.30, $\dot{\varepsilon}_m t_f$ increases with decreasing stress to around 150MPa and then decays rapidly as the stress is reduced further towards 50MPa, with the $\dot{\varepsilon}_m t_f$ values larger for P23 than for T23. Even so, the creep life increases as $\dot{\varepsilon}_m$ decreases, so the trends in t_f are approximately the inverse of those for $\dot{\varepsilon}_m$ in Figs 28 and 29.

Thus, plots were made of $\ln[t_f.\exp(-Q_c^*/RT)]$ against $\ln[-\ln(\sigma/\sigma_{TS})]$, assuming that $Q_c^* \cong 230\text{kJmol}^{-1}$. As recorded for the creep rate plots in Figs.28 and 29, this procedure split the data sets into three straight line segments for the P23 in Fig.31 and for T23 in Fig.32. For each straight line segment, the best value of Q_c^* was first determined before computing the best-fit results for k_1 and u in eqn.1. As evident from Table III, the same values of Q_c^* (with appropriate values of k_1 and u) were found over stress ranges identical to those identified from the creep rate measurements.

Comparisons of the data for $\dot{\varepsilon}_m$ (Figs.28 and 29) and t_f (Figs.30 and 32) shows that, for $0.55\sigma_{PS} > \sigma > 0.4\sigma_{PS}$, the creep rates are slower and the creep lives are longer than the figures predicted by extrapolation of results obtained for $\sigma > 0.55\sigma_{PS}$. Conversely, for $\sigma < 0.4\sigma_{PS}$, the creep rates are much faster and the creep lives far shorter than the

values produced by extrapolation of measurements from the $0.55\sigma_{PS}>\sigma>0.4\sigma_{PS}$ range when the bainite microstructure degrades to ferrite and coarse carbide particles along grain boundaries under low stresses above 873K. In addition, the log σ/log t_f relationships predicted by incorporating the k_1, u and Q_c* values in Table II into eqn.1 now fit extremely well with complex long term NIMS t_f data (Fig.2).

By recognizing that Q_c* values differ in different stress/temperature regimes using the variable k_1, u and Q_c* values in Table III also alters the allowable design stresses quoted on the earlier assumption of a fixed Q_c* value of 230kJmol^{-1} [23]. Thus, the new 100,000h stress rupture figures for P23 and T23 at 773K, 823K and 873K are listed in Table IV. While producing a relatively modest change in strength for the P23 samples, the very low strengths originally calculated [23] for T23 are now higher than those determined for P23 (Table IV). Moreover, the present strength estimates for P23 are similar to those reported [35] by applying the Larson-Miller method, which gave values of 114MPa at 848K, 90.2MPa at 873K and 66MPa at 898K. Additionally, the figures in Table IV confirm that the allowable creep strengths of both P23 and T23 are significantly better than those obtained by various groups for the Grade 22 products (Table I).

Tertiary Creep and Fracture Processes in Grade 23 Steels

Although creep occurs by the movement of dislocations within the grains and/or in the grain boundary regions under all stress/temperature conditions studied for the

P23 and T23 steels, the phenomena causing the onset of the tertiary stage and eventual fracture depend on the test conditions imposed.

An indication of the processes causing the onset of tertiary creep [36] is provided by the creep damage tolerance parameter (λ), namely [37]

$$\lambda = \left(\varepsilon_f - \varepsilon_p \right) / \dot{\varepsilon}_m t_f \cong \varepsilon_f / \dot{\varepsilon}_m t_f \qquad (7)$$

where ε_p is the primary creep strain. However, ε_p is sufficiently small so that (ε_f-ε_p) can be approximated by ε_f. With this approach, where $\lambda \cong 1$ to 2, tertiary creep begins as a consequence of grain boundary cavitation and intergranular crack development [38]. In contrast, when $\lambda > 2$, tertiary starts because of either neck formation or microstructural instability [38].

With P23, RoA $\cong 0.8$ (Fig.33), with RoA$>\varepsilon_f$ (Fig.34), so that $\lambda > 2$ suggests that neck formation at 723K and microstructural instability at 823K and above cause tertiary creep and transgranular failure. However, with T23, the differences in the stress and temperature dependencies of $\dot{\varepsilon}_m t_f$, ε_f and RoA (Figs.30, 34 and 33 respectively) indicate that the damage processes can differ significantly from those for P23.

As with P23, the data for T23 in Figs.30, 33 and 34 suggest that tertiary creep begins by necking at 773K and by microstructural instability at the higher temperatures, again leading to transgranular fracture under most test conditions. Yet, the rapid fall

in ε_f and RoA when $\sigma < 150$MPa indicates a change in failure mode to creep cavitation with T23. Even so, cavity development is then limited by grain boundary migration in the degraded T23 microstructures present at low stresses at 873K and above, so ε_f and RoA increase again during long-term tests at 898 and 923K (Figs 33 and 34). Hence, while failure of T23 can occur in an intergranular manner under some stress/temperature conditions, it appears that this grain boundary damage develops largely during the tertiary stage without affecting the value of the $\dot{\varepsilon}_m t_f$ product. Consequently, the stress and temperature dependencies of $\dot{\varepsilon}_m t_f$ are essentially similar for P23 and T23 (Fig.30).

Creep Fracture of Grade 24 steels

The NIMS results for Gr.24 steels [8] in the non-stress relieved and stress relieved states do not exceed 20,000h (NIMS designations VdA and VdB respectively). Even so, expressing the data sets in terms of eqn.(4), as shown in Figs.35 and 36, a decrease occurs from $n \cong 22$ to $n \cong 5$ as the stress is reduced from around 500MPa to almost 100MPa and the temperature is raised from 723 to 973K. As the n value decreased, Q_c increased from 295 to 551 kJmol^{-1}. However, while both products received the same initial heat-treatment schedules of 1293K for 7h before water quenching and then 11h at 968K before air cooling, the stress relieved samples were subsequently air cooled after 10h at 898K, followed by air cooling after 30h at 978K [8]. This additional stress relieving treatment tempers the initial bainitic structure, such that the non-stress relieved material was significantly more creep fracture resistant than the stress relieved Gr.24 steel (Figs.35 and 36).

Applying eqn.(1) to the t_f values obtained for both products, the $\ln[t_f.\exp(-Q_c^*/RT)]$ against $\ln[-\ln(\sigma/\sigma_{TS})]$ plots again seemed to show three intersecting straight line segments, although there were relatively few tests carried out in the lowest stress regime for the stress-relieved samples (Figs.37 and 38). Subsequent analyses of each straight line segment then gave the k_1, u and Q_c^* values in Table V. Once more, with the non-stress relieved steel, Q_c^* falls from around 280kJmol^{-1} to about 230kJmol^{-1} as the applied stress was lowered from above to below $0.8\sigma_{PS}$ ($\cong 0.7\sigma_{TS} \cong \sigma_Y$), with a subsequent rise to Q_c^*=280kJmol^{-1} when the stress was further reduced to below $0.6\sigma_{PS}$ ($\cong 0.55\sigma_{TS}$). With the stress-relieved product, the same Q_c^* changes occurred on lowering the stress from above to below $0.65\sigma_{PS}$ ($\cong 0.6\sigma_{TS}$) and then to below $0.45\sigma_{PS}$ ($\cong 0.4\sigma_{TS}$).

The plots in Figs.37 and 38 are very similar in form to those found for the Gr.22 tube (Fig.12) and Gr.23 pipe and tube samples (Figs.31 and 32), with comparable Q_c^* values found for these products in Tables V, II and III. Thus, the two Gr.24 materials appear to display the same creep deformation modes, namely, dislocation generation and movement within the grains as well as the grain boundary zones when $\sigma>\sigma_Y$, dislocation movement restricted to the grain boundary regions when $\sigma<\sigma_Y$, with dislocation activity within the grains being restored when the bainitic microstructures degrade to ferrite and coarse carbide particles during long-term tests in the low stress regimes.

While the detailed dislocation processes governing creep strain accumulation differ slightly in different (σ/σ_{PS}) regimes, the fracture mode does not change over the entire stress/temperature ranges covered for the two Gr.24 steels. Thus, RoA>0.8 while $\varepsilon_f \cong$ 0.2-0.3 (Figs.39 and 40 respectively). So, with RoA/$\varepsilon_f \cong$ 3-4, creep failure always takes place after extensive necking in a transgranular manner. Then, using eqn.(1) with the k_1, u and Q_c^* values in Table V, the stress rupture behaviour is very well represented (Figs.35 and 36), giving the 100,000h creep rupture strengths for the Gr.24 steels in Table VI. Thus, the allowable creep strengths for the non-stress relieved and stress relieved Gr.24 materials (Table VI) are substantially greater than the values for Gr.22 (Table I) and broadly comparable with the long-term strengths for Gr.23 (Table IV).

Conclusions

1. Although power law descriptions of 'steady state' creep have been used for well over 50 years, the present analysis of data obtained for bainitic Grades 22, 23 and 24 steels confirm that this approach should be seriously reconsidered. Specifically, with very few exceptions, the creep curves display a decaying primary rate, giving way to an accelerating tertiary rate, producing a minimum rather than a steady state rate. The observed behaviour patterns should therefore be interpreted in terms of the deformation processes governing creep strain accumulation and the damage phenomena causing the onset of the tertiary stage and eventual fracture.

2. In line with previous studies [16,30], the present review suggests that no transition takes place from dislocation to diffusional creep mechanisms with decreasing applied stress. Instead, dislocation creep processes are rate controlling at all stress levels, even though the detailed dislocation processes vary in different stress/temperature regimes. Thus, with Gr.22, 23 and 24 steels, the creep and creep fracture properties differ above and below $\sigma \cong \sigma_Y$. When $\sigma > \sigma_Y$, so that the initial strain on loading (ε_0) has both elastic and plastic components, creep is controlled by the generation and movement of dislocations within the grains. In contrast, when $\sigma < \sigma_Y$, so that ε_0 has essentially only an elastic component, new dislocations are not generated within the grains, so creep occurs within the grain boundary zones, i.e. by grain boundary sliding and associated deformation in grain regions adjacent to the boundaries. Hence, the creep rates when $\sigma < \sigma_Y$ are slower and the creep lives are longer than expected by direct extrapolation of $\dot{\varepsilon}_m$ and t_f data obtained when $\sigma > \sigma_Y$.

3. With Gr.22 tube and Gr.23 pipe and tube, as well as with Gr.24 steels in the non-stress relieved and stress relieved conditions, a further change in creep and creep rupture behaviour occurs when σ falls to low σ_{TS} (σ_{PS}) values. With these materials, a transformation from bainite to ferrite and coarse carbide particles takes place in long-term tests at the highest creep temperatures. In these cases, because of the loss of creep resistance caused by this transformation, the $\dot{\varepsilon}_m$ values are faster and the t_f values are shorter when σ_{TS} is very low than would be predicted by extrapolation of data collected at intermediate σ_{TS} levels.

4. Applying eqn.(1) to the t_f values available for the Gr.22, 23 and 24 steels, the values of k_1, u and Q_c^* also differ in different stress/temperature regimes. Specifically, $Q_c^* \cong 280\text{kJmol}^{-1}$ when creep occurs by the generation and movement of dislocations within the grains for $\sigma > \sigma_Y$, whereas $Q_c^* \cong 230\text{kJmol}^{-1}$ when creep is confined to the grain boundary zones when $\sigma < \sigma_Y$. These Q_c^* values coincide with the activation energies for lattice diffusion within the bainitic grains and within the grain boundary zones respectively. With the lower creep resistance of these materials when the bainitic-ferrite transformation occurs at very low σ_{TS} and σ_{PS} values, dislocation activity is restored within the grains, so Q_c^* rises again towards 280kJmol^{-1}.

5. Under most conditions studied for the Gr.22, 23 and 24 steels, RoA$>\varepsilon_f$ with large values of RoA and ε_f showing that failure occurs in a transgranular manner after extensive necking. However, with the quenched/tempered Gr.22 steel and the Gr.23 tube under selected stresses at intermediate temperatures, low values of RoA and ε_f signify that intergranular failure modes are displayed. Even so, it appears that the grain boundary cavities and cracks form during the tertiary stage, so that no significant change occurs in the stress dependencies of the creep life.

6. Applying eqn.(1) to the NIMS stress rupture data for Gr.22,23 and 24 steels, utilizing the k_1, u and Q_c^* values in Tables II, III and V, allows the 100,000h stress rupture properties to be predicted accurately from t_f measurements from tests lasting less than 5000h. The 100,000h creep life estiamtes for all heat treatments given to the three bainitic steels are listed in Tables I, IV and VI. These results demonstrate that the long-term creep strengths are greater

for Gr.23 and Gr.24 than for Gr.22, so that replacement of Gr.22 by either Gr.23 or 24 can allow component wall thicknesses to be reduced and the construction cost of new electricity generating plant to be reduced significantly.

References

1. J.D. Parker. The Grade 22 low alloy steel handbook, 2005, Palo Alto, CA, EPRI.

2. NIMS Creep Data Sheet no.36B. 2003.

3. NIMS Creep Data Sheet no.11B. 1997.

4. NIMS Creep Data Sheet no.3B. 1986.

5. NIMS Creep Data Sheet no. M-4. Metallographic atlas of long-term crept materials. 2005.

6. 'Boiler and pressure vessel code', 2004, New York, ASME.

7. NIMS Creep Data Sheet no.54. 2008. Data sheets on the elevated-temperature properties of 2.25Cr-1.6W steel tubes for power boilers and 2.25Cr-1.6W steel pipe for high-temperature service.

8. NIMS Creep Data Sheet no.53. 2007. Data Sheets on the elevated-temperature properties of 2.25Cr-1Mo-0.3V high strength chromium-molybdenum alloy steel forgings for pressure vessels under high temperature service.

9. J. Hald. Mater. High Temp. 2004, Vol. 41, pp. 41-46.

10. S.R.Holdsworth, M.Askins, A. Baker, E. Gariboldi, R. Sandstrom, M. Schwiersheer and S. Spigarelli: in 'Creep and fracture in high temperature

components – design and life assessment issues' (ed. I.A. Shibli, S.R. Holdsworth, G. Merckling) 2005, London, DEStech, pp. 380-393.

11. G. Merckling: in 'Creep and fracture in high temperature components – design and life assessment issues' (ed. I.A. Shibli, S.R. Holdsworth, G. Merckling) 2005, London, DEStech, pp. 3-19.

12. J.C Vailant, R. Vandenberghe, B. Hahn, H. Heuser and C. Jochum: in 'Creep and fracture in high temperature components – design and life assessment issues' (ed. I.A. Shibli, S.R. Holdsworth, G. Merckling) 2005, London, DEStech, pp. 87-96.

13. W. Bendick and J. Gabrel: in 'Creep and fracture in high temperature components – design and life assessment issues' (ed. I.A. Shibli, S.R. Holdsworth, G. Merckling) 2005, London, DEStech, pp. 406-418.

14. K. Maruyama and J.S. Lee: in 'Creep and fracture in high temperature components – design and life assessment issues' (ed. I.A. Shibli, S.R. Holdsworth, G. Merckling) 2005, London, DEStech, pp. 372-379.

15. K. Kimura: in 'Creep and fracture in high temperature components – design and life assessment issues' (ed. I.A. Shibli, S.R. Holdsworth, G. Merckling) 2005, London, DEStech, pp. 1009-1022.

16. B. Wilshire and A. Battenbough: Mater. Sci. Eng. A. 2007, Vol. A443, pp. 156-166.

17. B. Wilshire and P.J. Scharning: Int. J. Press. Vessels. Pip. 2008, Vol. 85, pp. 739-743.

18. B. Wilshire and P.J. Scharning: Mater. Sci. Technol. 2008, Vol. 24, pp. 1-9.

19. B. Wilshire and P.J. Scharning: Int. Mater. Rev. 2008, Vol. 53, pp. 91-104.

20. B. Wilshire and P.J. Scharning: J. Mater. Sci. 2008, Vol. 43, pp. 3992-4000.

21. K. Sawada, M. Fujitsuka, M. Tabuchi, K. Kimura : in 'Sec. ECCC Conf on Creep and fracture in high temperature components – design and life assessment issues' (ed. I.A. Shibli, S.R. Holdsworth) 2009, Zurich, DEStech, pp. 79-92.

22. F.R. Larsson and J. Miller: Trans ASME, 1952, Vol. 74, pp. 765-775.

23. M.T. Whittaker and B. Wilshire: Mater. Sci. Eng. A, 2010, Vol. 527, pp. 4932-4938.

24. M.T. Whittaker and B. Wilshire: Mater. Sci. Tech. 2011, Vol. 27, pp. 642-647.

25. M.F. Ashby: Acta Metall. 1972, Vol. 20, pp. 887-897.

26. H.J. Frost and M.F. Ashby: Deformation Mechanism Maps. London, Pergamon Press, 1982.

27. R.W. Evans and B. Wilshire: Creep of metals and alloys. London, The Institute of Metals, 1985.

28. F.R.N. Nabarro: Mater. Sci. Eng. A. 2004, Vol. 659A, pp. 387-389.

29. E. Arzt: Res. Mech. 1991, Vol. 31, pp. 399-431.

30. B. Wilshire and M.T. Whittaker. Acta mater. 2009, Vol. 57, pp. 4115-4124.

31. P.W. Davies, J.D. Richards and B. Wilshire: The Inst. Metals. 1961-62, Vol. 90, pp. 431-434.

32. R.L. Squires, R.T. Weiner and M. Phillips. J. Nuel. Mater. 1963, Vol. 8, pp. 77-80.

33. J.E. Harris and R.B. Jones: J. Nucl. Mater. 1963, Vol. 10, pp. 360-362.

34. J.G. Park, D.Y. Lee and J. Choi: J. Mater. Sci. 1996, Vol. 31, pp. 2719-2723.

35. M. Ingarashi, M. Yoshizawa, H. Matsuo, O. Miyahara and A. Iseda: Mater. Sci. Eng. A. 2009, Vol. 510-511A, pp. 104-109.

36. M.F. Ashby and B.F. Dyson: in Advances in fracture research (ed. S.R. Valluri),

1, Oxford, Pergamon Press, 1984, pp. 3-30.

37. F.A. Leckie and D.R. Hayhurst: Acta metal. 1977, Vol. 25, pp. 1059-1070.

38. B. Wilshire and H. Burt: Z. Metallk. 2005. Vol. 96, pp. 552-557.

FIGURES
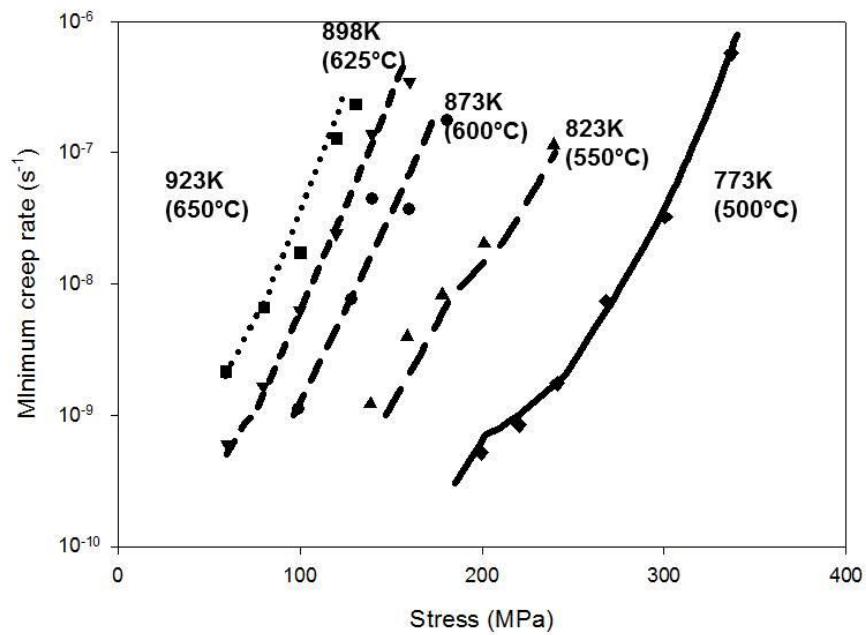
Figure 1: The stress dependence of the minimum creep rate at 773-923K (500-650°C) for 2.25Cr-1.6W steel pipe (Grade 23). The lines are drawn after analysing the results according to eqn. (2), using the data in Table III.
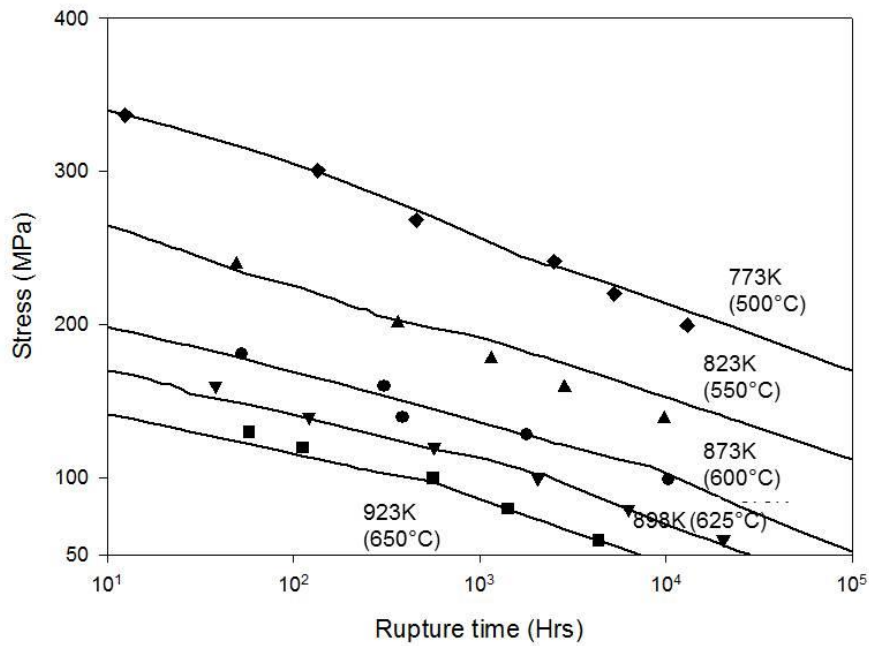
Figure 2: The stress dependence of the creep life at 773-923K (500-650°C) for 2.25Cr-1.6W steel pipe (P23). The lines are drawn after analysing the results according to eqn. (1), using the data in Table III.
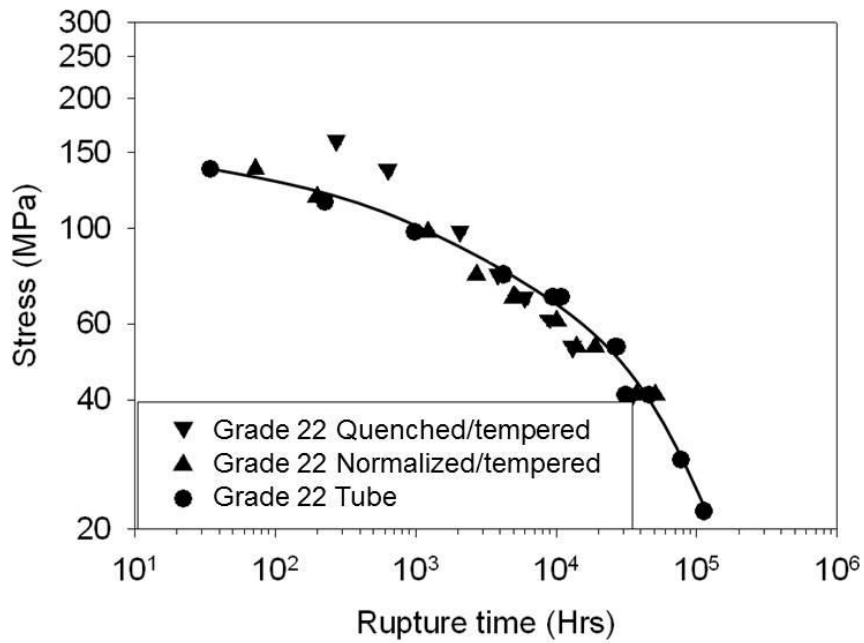
Figure 3: The stress dependence of the creep life at 873K (600°C) for Gr.22 tube, normalized-tempered and quenched-tempered steels.
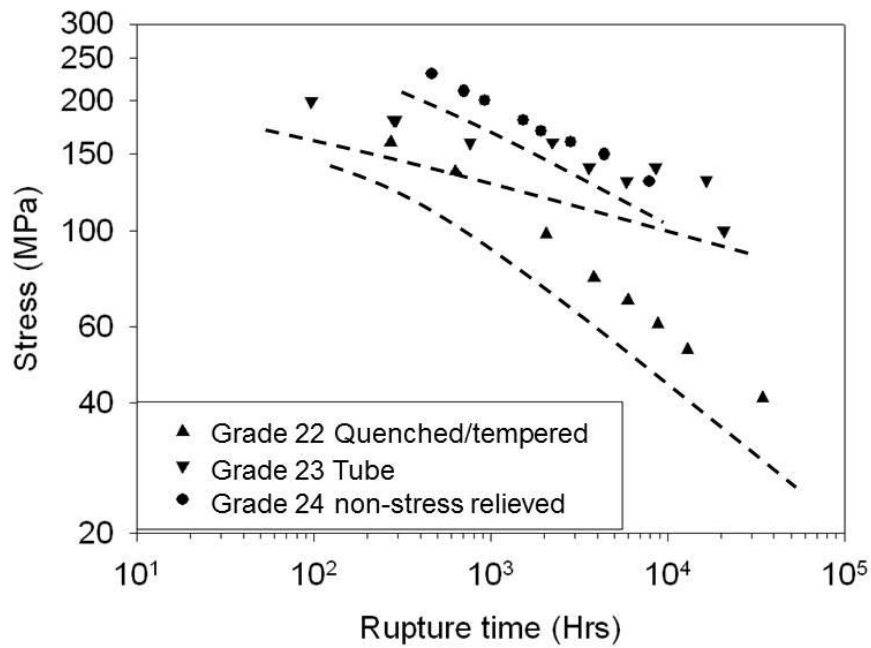
Figure 4: The stress dependence of the creep life at 873K (600°C) for Gr.22, 23 and 24 steels.
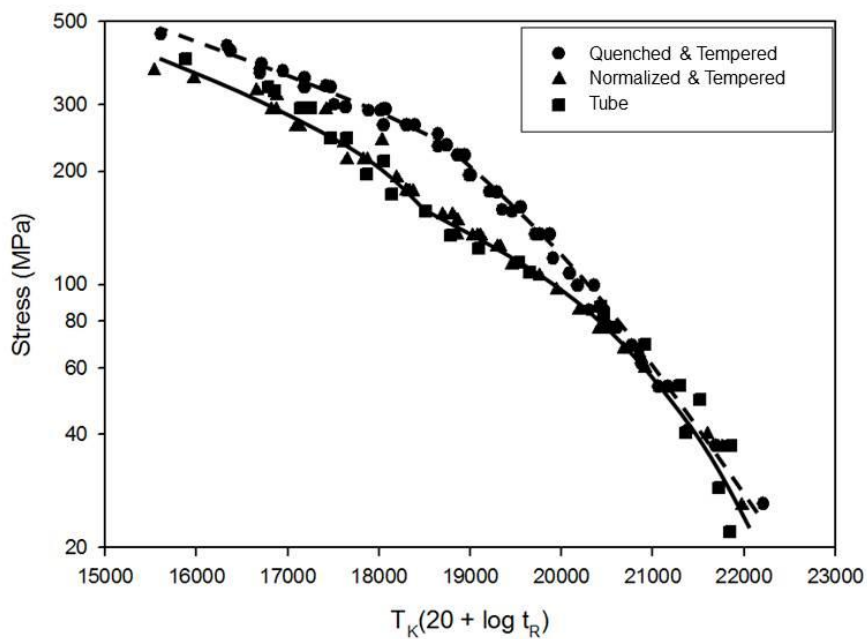
Figure 5: The stress dependence of the creep life at 873K (600°C) for Gr.22, 23 and 24 steels.
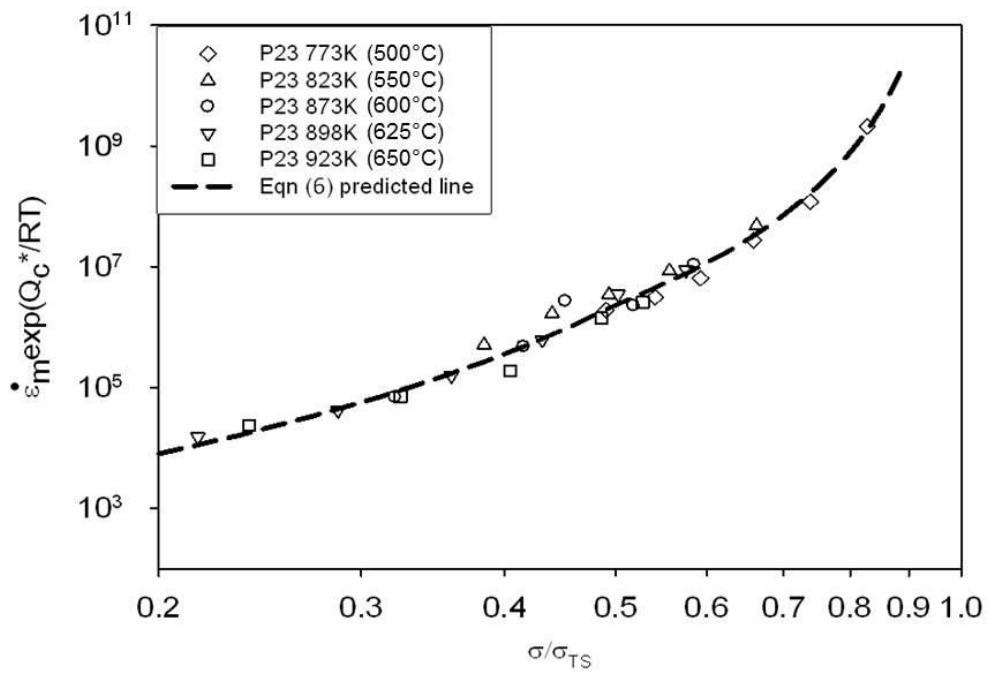
Figure 6: The dependence of $\log[\dot{\varepsilon}_m \cdot \exp(230{,}000/RT)]$ on $\log(\sigma/\sigma_{TS})$ at 773-923K (500-650°C) for 2.25Cr-1.6W steel pipe (P23) using eqn.(6).
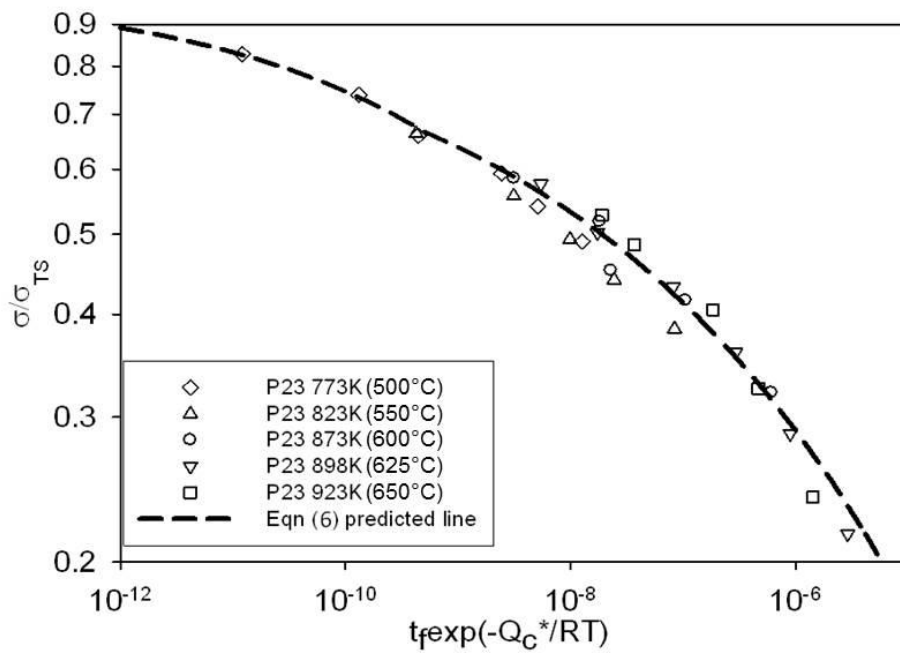
Figure 7: The dependence of $\log[t_f \cdot \exp(-230{,}000/RT)]$ on $\log(\sigma/\sigma_{TS})$ at 773-923K (500-650°C) for 2.25Cr-1.6W steel pipe (P23) using eqn.(6).
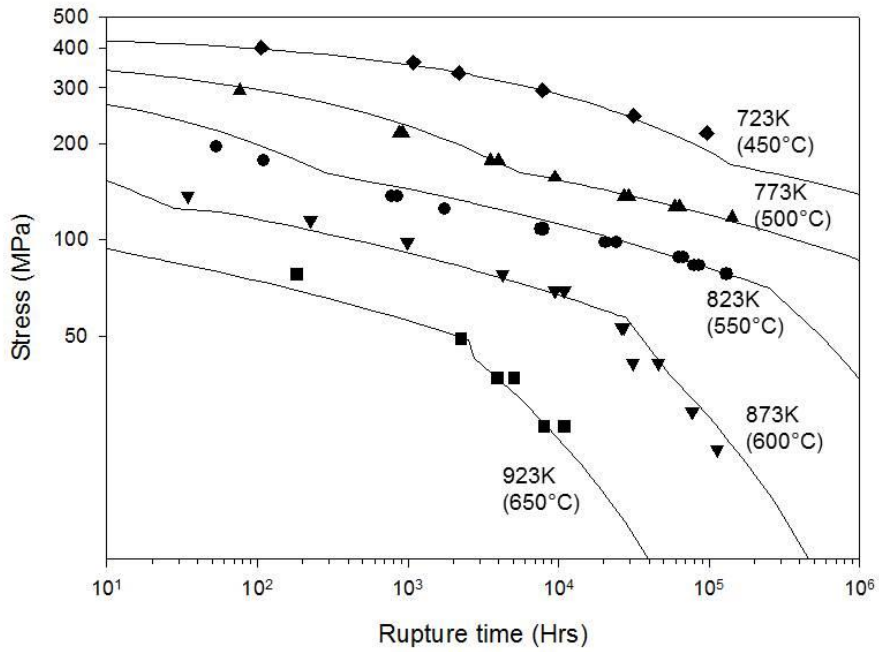
Figure 8: The stress dependence of the creep life at 723-923K (450-650°C) for 2.25Cr-1Mo steel tube (T22). The lines are drawn after analysing the results according to eqn. (1), using the data in Table II.
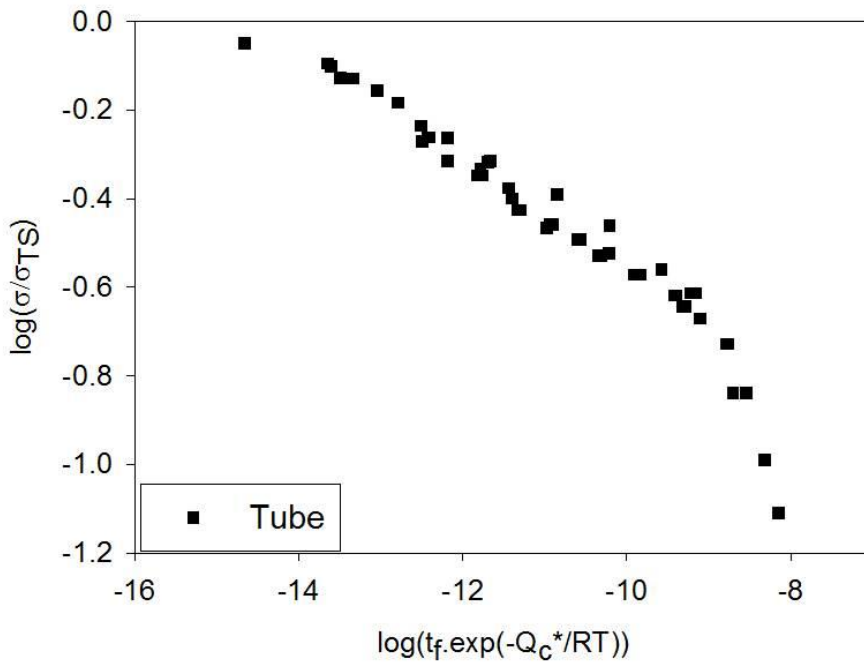
Figure 9: The dependence of $\log[t_f \cdot \exp(-280{,}000/RT)]$ on $\log(\sigma/\sigma_{TS})$ at 723-923K (450-650°C) for 2.25Cr-1Mo steel tube (T22) using eqn. (6).
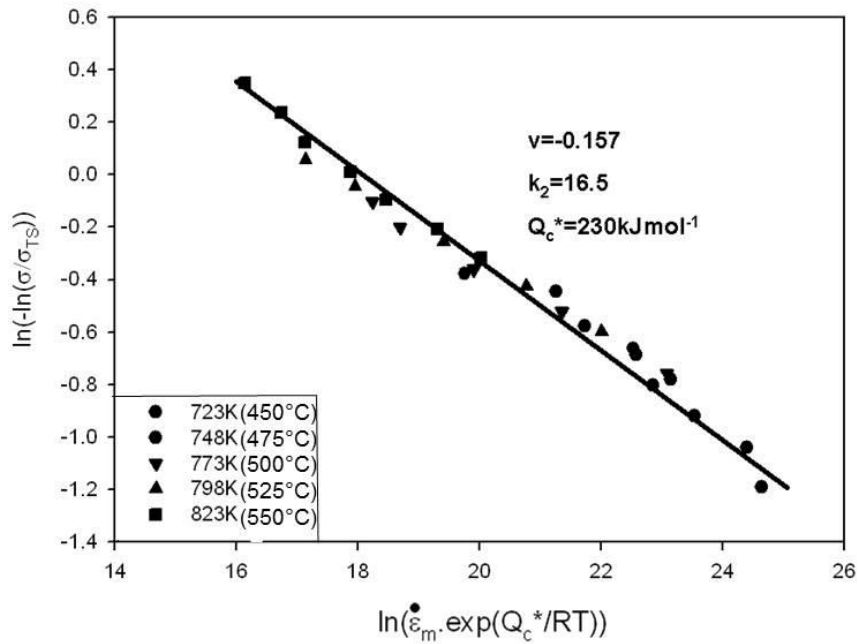
Figure 10: Adopting eqn.(2), the best k_2, v and Q_c^* values are determined by plotting $\ln[\dot{\varepsilon}_m .\exp(Q_c^*/RT)]$ against $\ln[-\ln(\sigma/\sigma_{TS})]$ for the quenched-tempered Gr.22 plate.
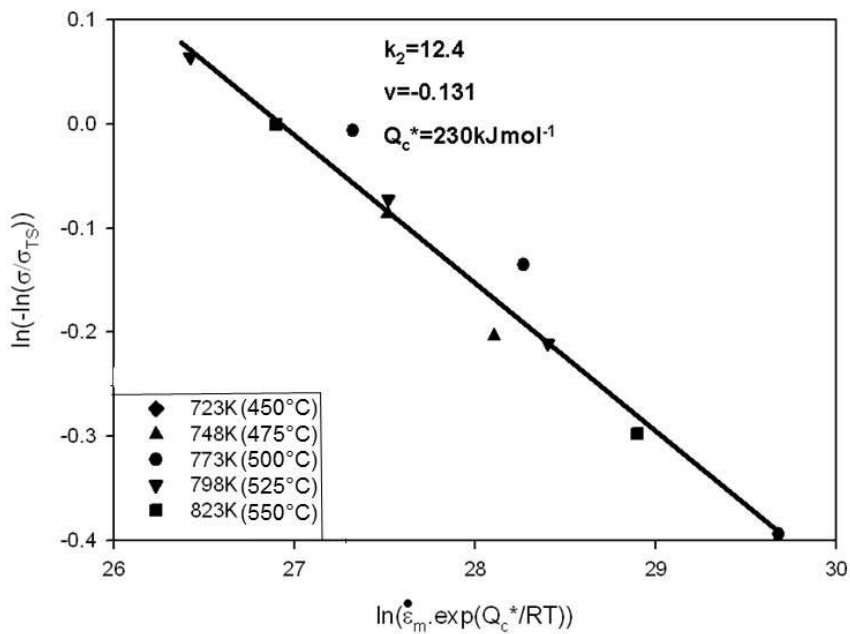
Figure 11: Adopting eqn.(2), the best k_2, v and Q_c^* values are determined by plotting $\ln[\dot{\varepsilon}_m .\exp(Q_c^*/RT)]$ against $\ln[-\ln(\sigma/\sigma_{TS})]$ for the normalized-tempered Gr.22 plate.
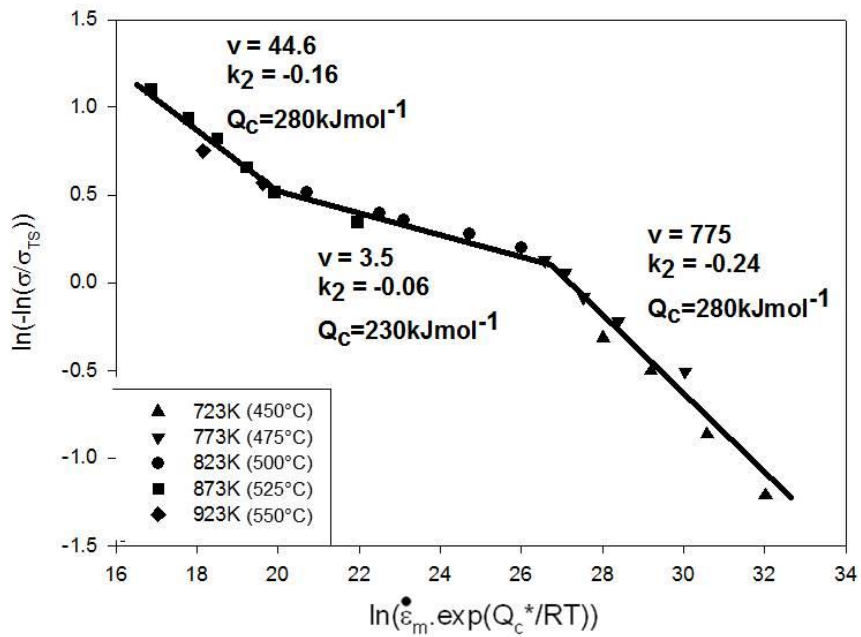
Figure 12: Adopting eqn.(2), the best k_2, v and Q_c^* values are determined by plotting $\ln[\dot{\varepsilon}_m.\exp(Q_c^*/RT)]$ against $\ln[-\ln(\sigma/\sigma_{TS})]$ for Gr.22 tube.
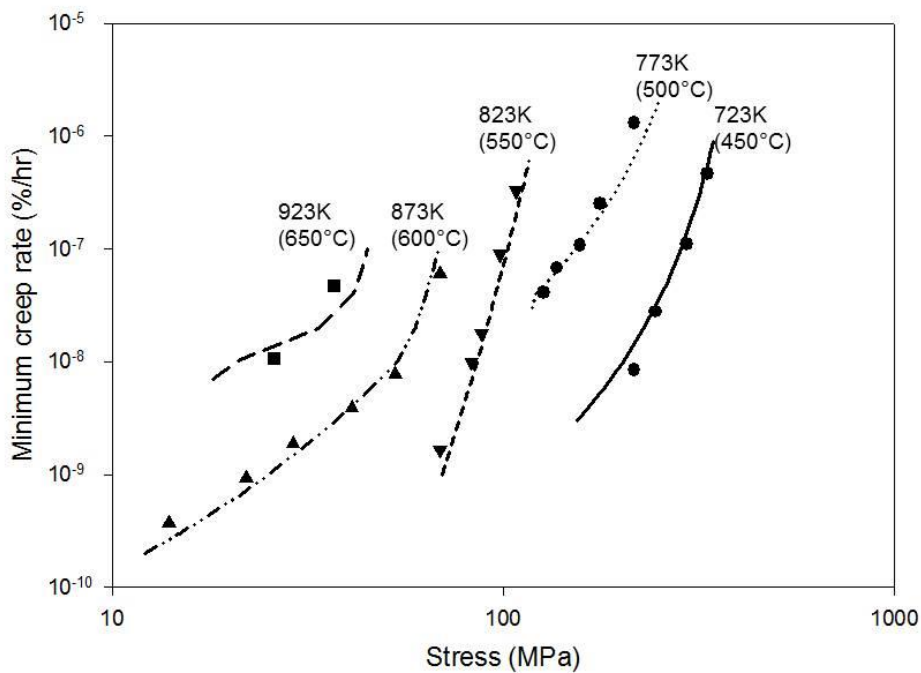
Figure 13: The dependence of $\log \dot{\varepsilon}_m$ on $\log \sigma$, with the predicted solid curves drawn by using eqn. (2) with the k_2, v and Q_c^* values found over different (σ/σ_{TS}) ranges for Gr.22 tube in Table II.
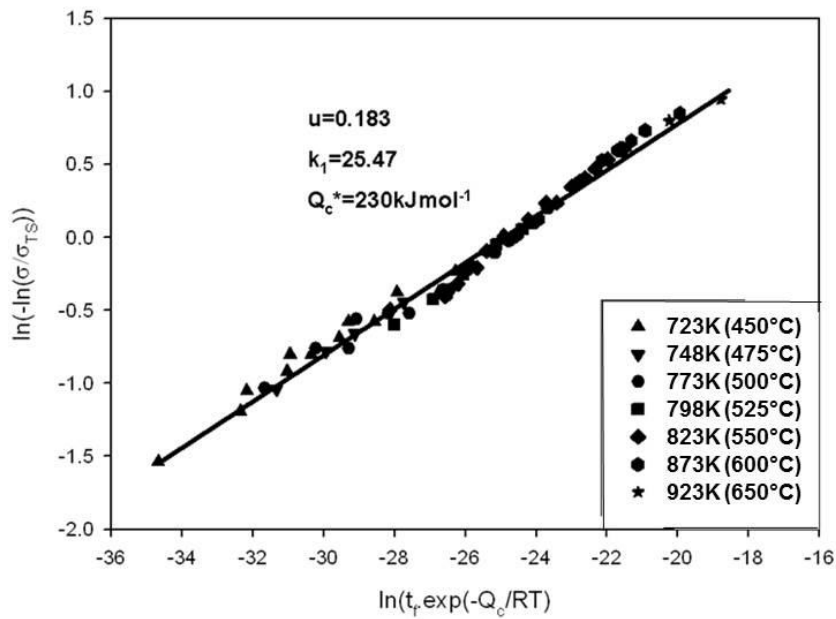
Figure 14: Adopting eqn.(1), the k_1, u and Q_c^* values are determined by plotting of $\ln[t_f.\exp(-Q_c^*/RT)]$ against $\ln[-\ln(\sigma/\sigma_{TS})]$, for quenched-tempered Gr.22 plate.
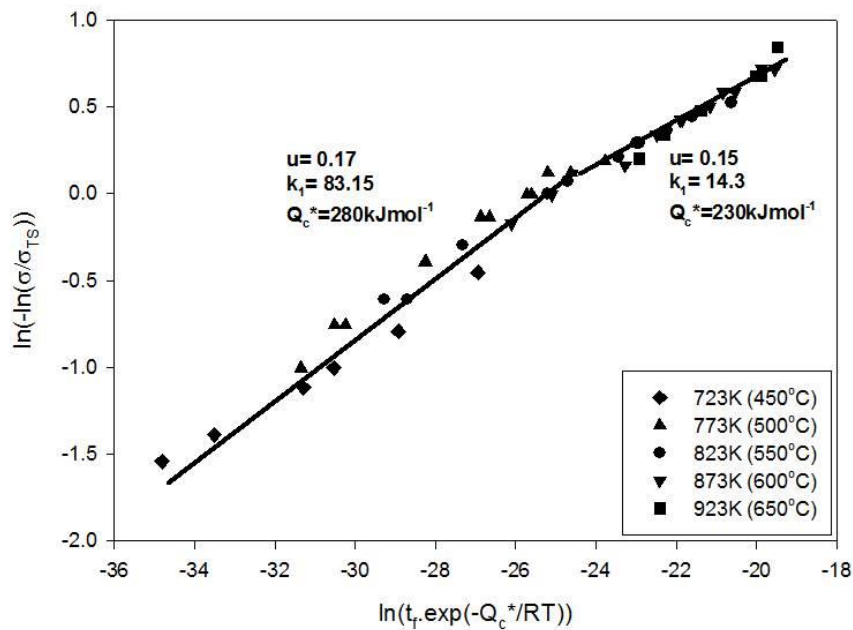
Figure 15: Adopting eqn.(1), the k_1, u and Q_c^* values are determined by plotting of $\ln[t_f.\exp(-Q_c^*/RT)]$ against $\ln[-\ln(\sigma/\sigma_{TS})]$, for normalized-tempered Gr.22 plate.
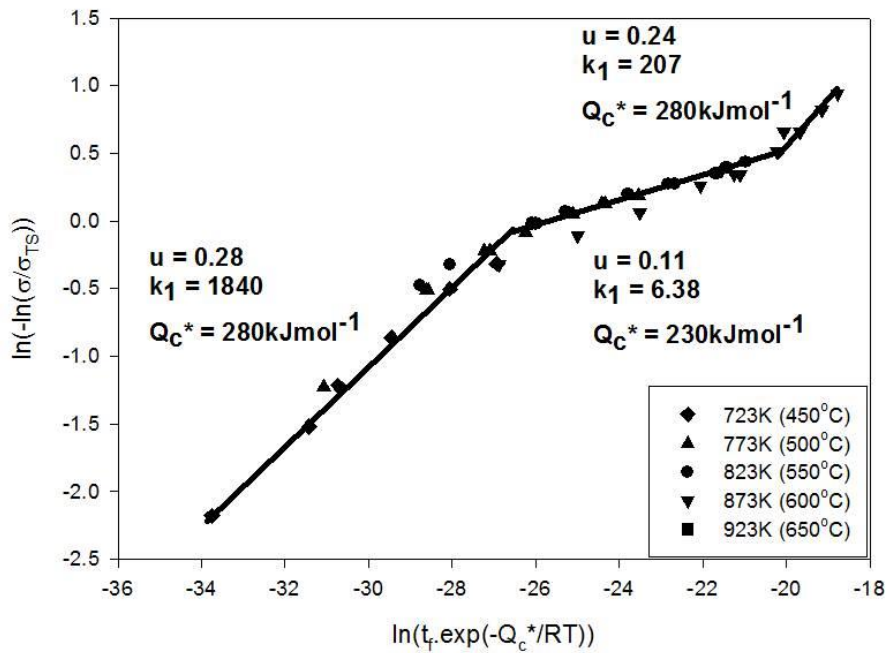
Figure 16: Adopting eqn.(1), the k_1, u and $Q_c{}^*$ values are determined by plotting of $\ln[t_f.\exp(-Q_c{}^*/RT)]$ against $\ln[-\ln(\sigma/\sigma_{TS})]$, for Gr.22 tube.
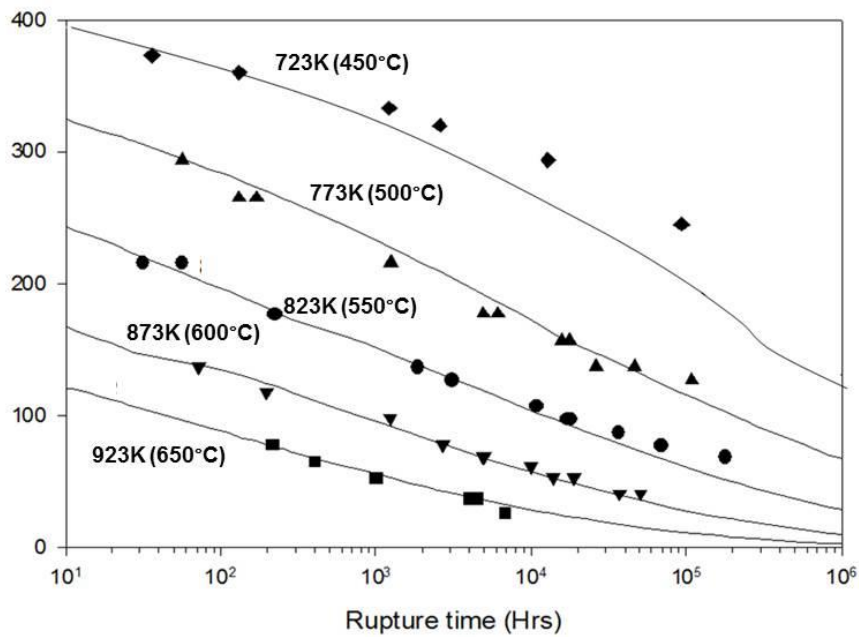
Figure 17: The stress dependence of the creep life at 723-923K (450-650°C) for the 2.25Cr-1Mo Gr.22 steel in the normalized-tempered condition. The solid lines were predicted using eqn. (1) with the data in Table II.
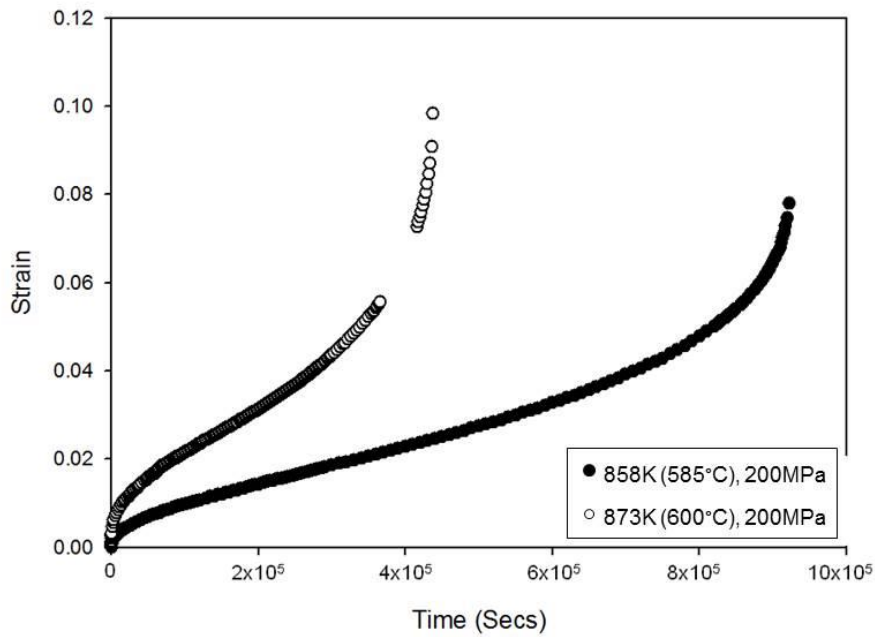
Figure 18: Creep strain against time curves obtained in constant-stress tests for Grade 22 steel under a stress of 200MPa at 858 and 873K (585 and 600°C).
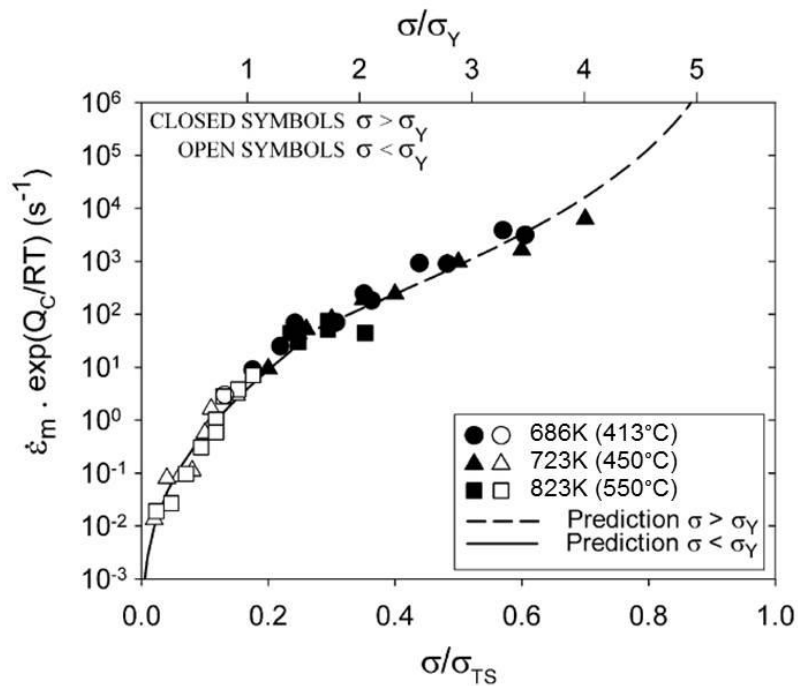
Figure 19: The dependence of log [$\dot{\varepsilon}_m$ .exp (Q_c*/RT)] on (σ/σ_{TS}) and (σ/σ_Y) at 686 to 823K (413 to 550°C) for polycrystalline copper, where Q_c*=110kJmol[-1]. Using eqn.(2), the broken curve predicts the results for $\sigma>\sigma_Y$, while the solid line predicts the behaviour for $\sigma<\sigma_Y$ [16].
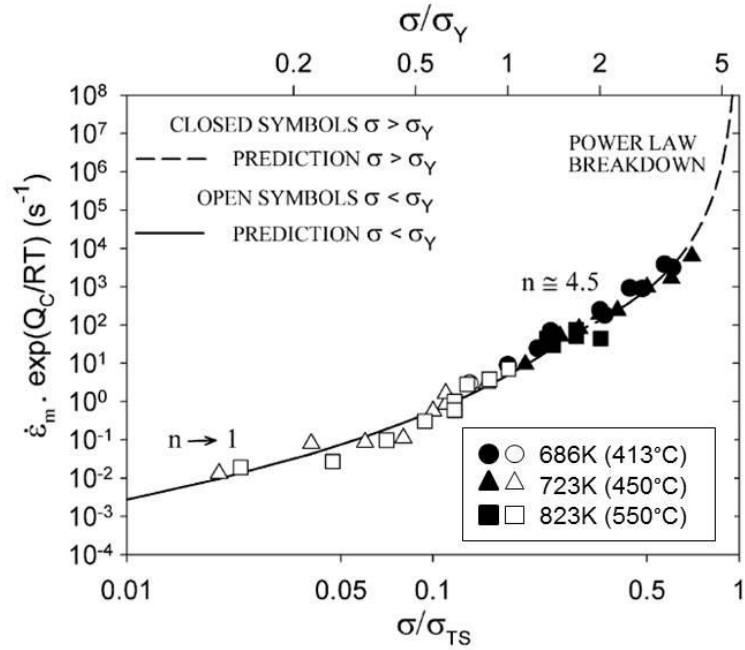
Figure 20: The dependence of log [$\dot{\varepsilon}_m$.exp (Q_c*/RT)] on log(σ/σ_{TS}) and log(σ/σ_Y) at 686 to 823K (413 to 550°C) for polycrystalline copper, where Q_c*=110kJmol^{-1}. The power law behaviour patterns, captured from the predicted curves in Fig.19 using eqn.(2), are shown as the broken curve for $\sigma>\sigma_Y$ and the solid curve for $\sigma<\sigma_Y$ [16].
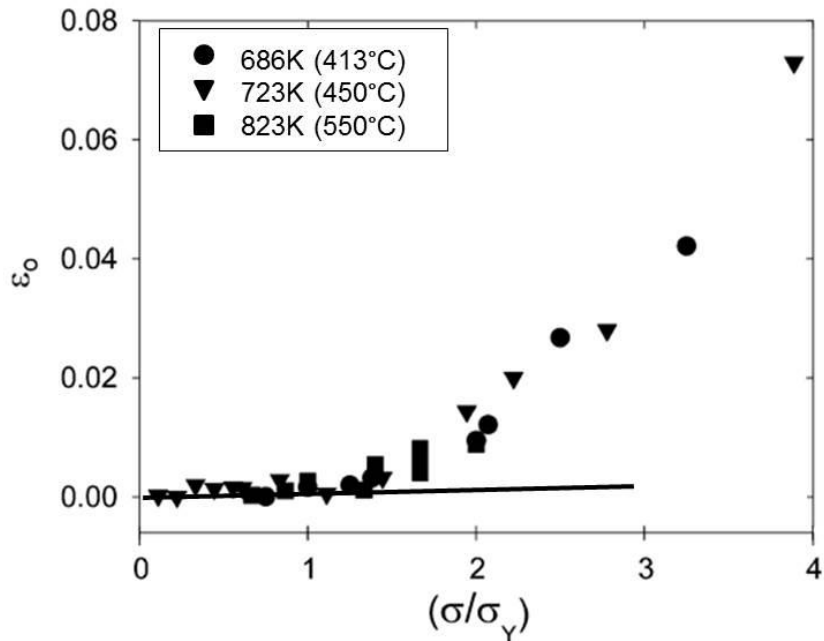
Figure 21: The dependence of the initial strain on loading (ε_0) on the normalized stress, (σ/σ_Y) at 686-823K (413-550°C) for polycrystalline copper [16].
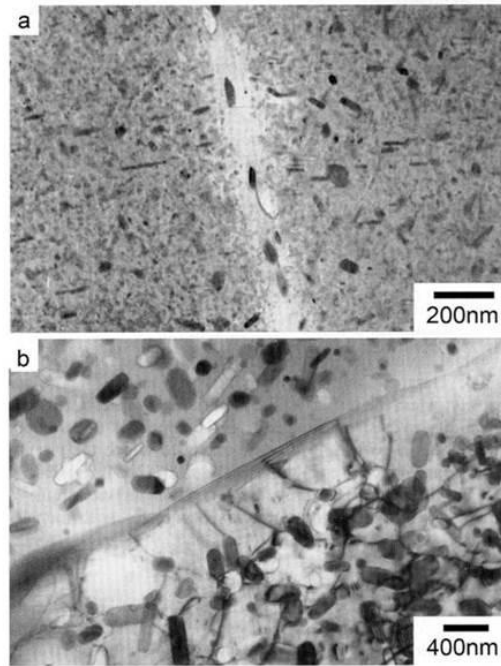
Figure 22: Transmission electron micrographs obtained for the aluminium alloy 7010 (a) in the as-received condition and (b) after 1915ks (532h) under a stress of 75MPa at 473K (200°C) [20].
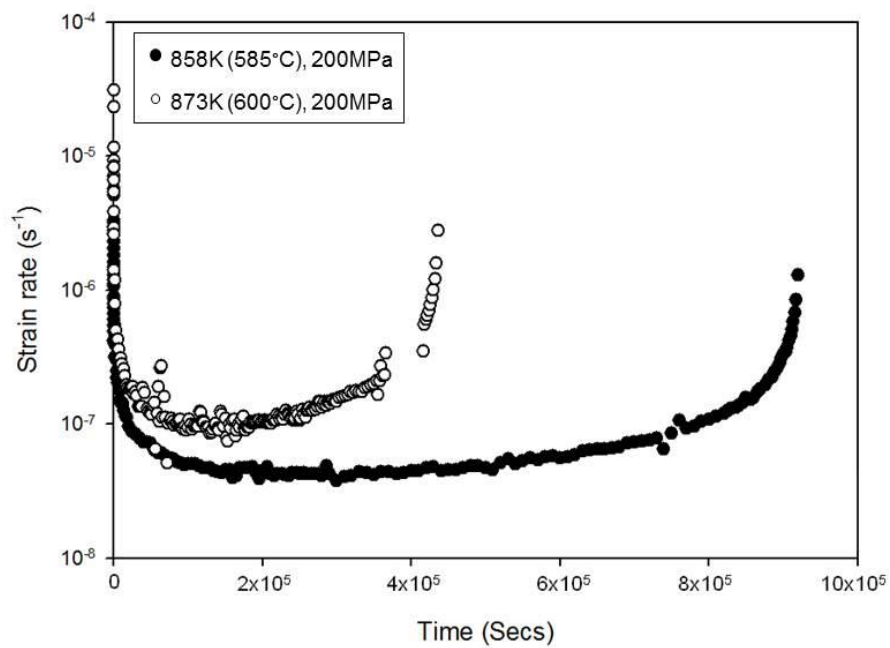
Figure 23: Creep strain rate against time curves obtained in constant-stress tests for Grade 22 steels under a stress of 200MPa at 858 and 873K (585 and 600°C).
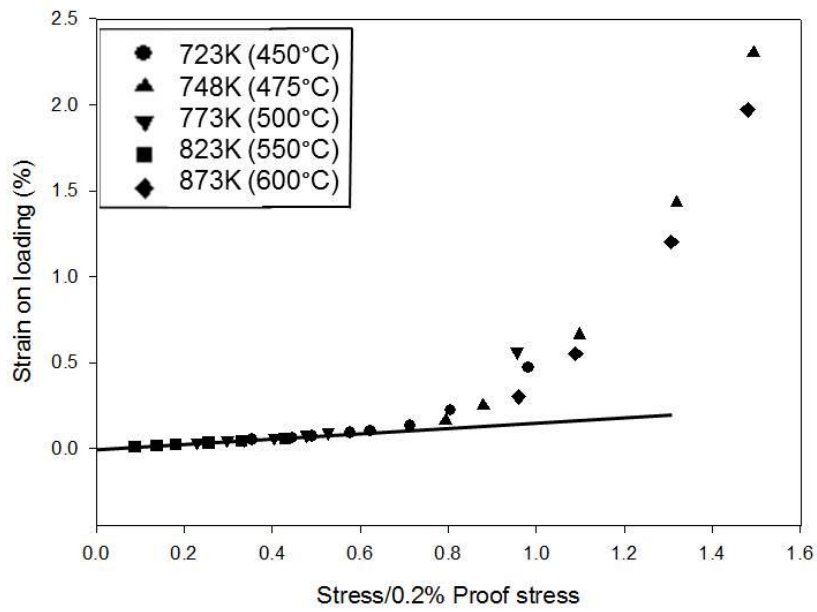
Figure 24: The variation of the initial strain on loading (ε_0) with (σ/σ_{PS}) for Gr.22 tube at 673-923K (400-650°C).
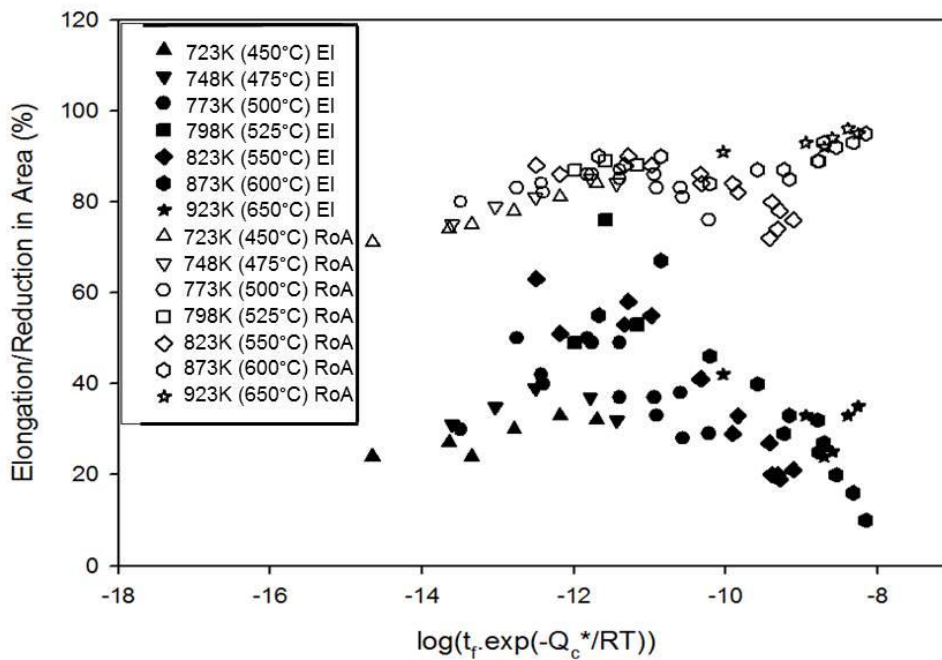
Figure 25: The dependencies of the reduction in area (RoA) and total strain to failure (ε_f) on log[t_f .exp ($-Q_c^*$/RT)], using the Q_c^* values in Table II, for Grade 22 steel tube.
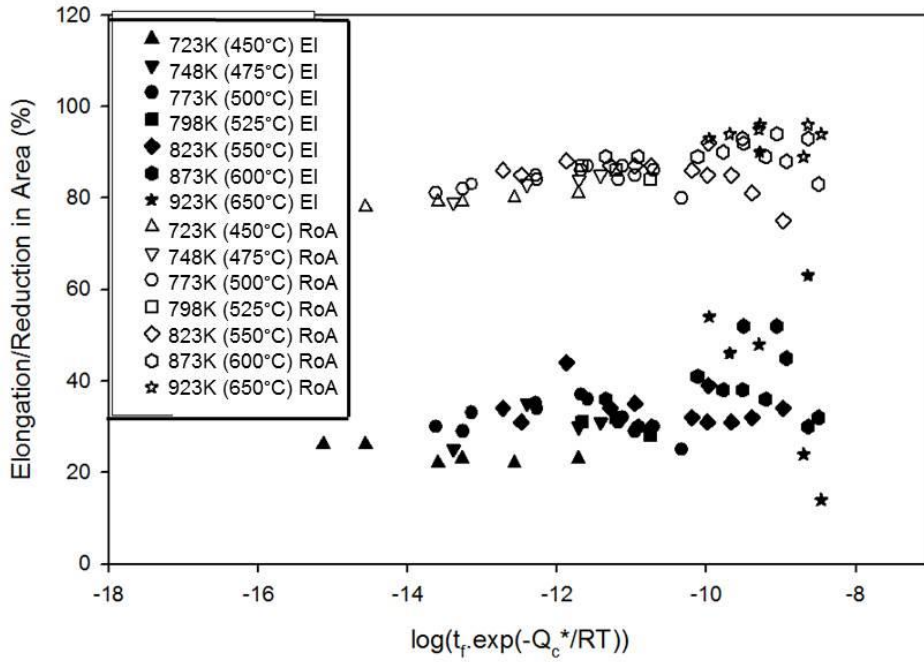
Figure 26: The dependencies of the reduction in area (RoA) and total strain to failure (ε_f) on $\log[t_f \cdot \exp(-Q_c^*/RT)]$, using the Q_c^* values in Table II, for Grade 22 normalized-tempered steel.
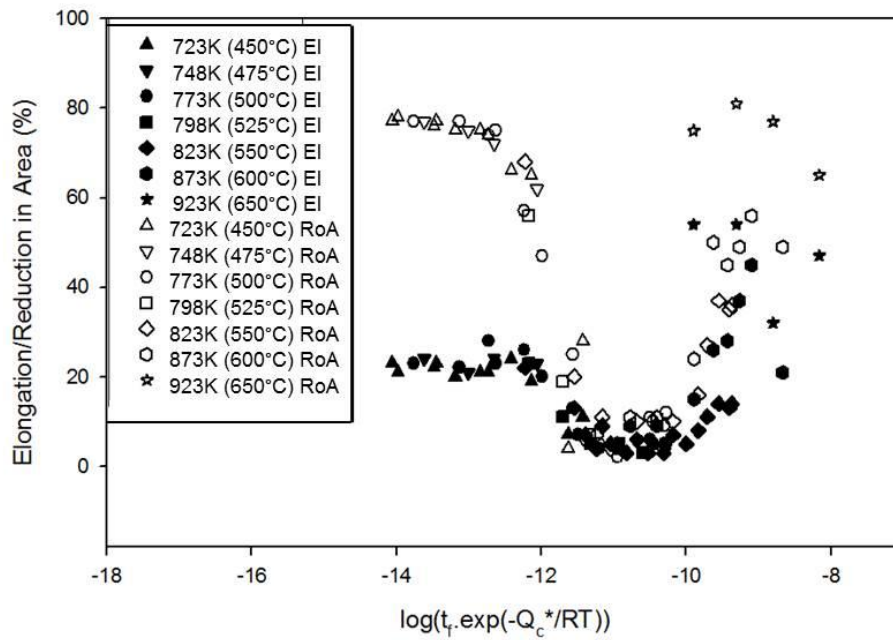
Figure 27: The dependencies of the reduction in area (RoA) and total strain to failure (ε_f) on $\log[t_f \cdot \exp(-Q_c^*/RT)]$, using the Q_c^* values in Table II, for Grade 22 quenched-tempered steel.
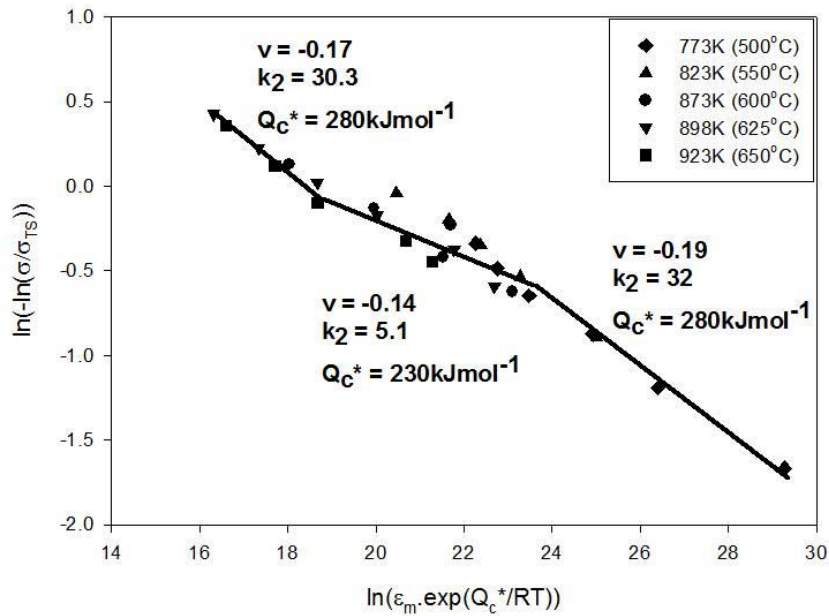
Figure 28: Adopting eqn.(2), plotting $\ln[\dot{\varepsilon}_m \cdot \exp(Q_c^*/RT)]$ as functions of $\ln[-\ln(\sigma/\sigma_{TS})]$, gives the k_2, v and Q_c^* figures listed in Table III for P23 steel.
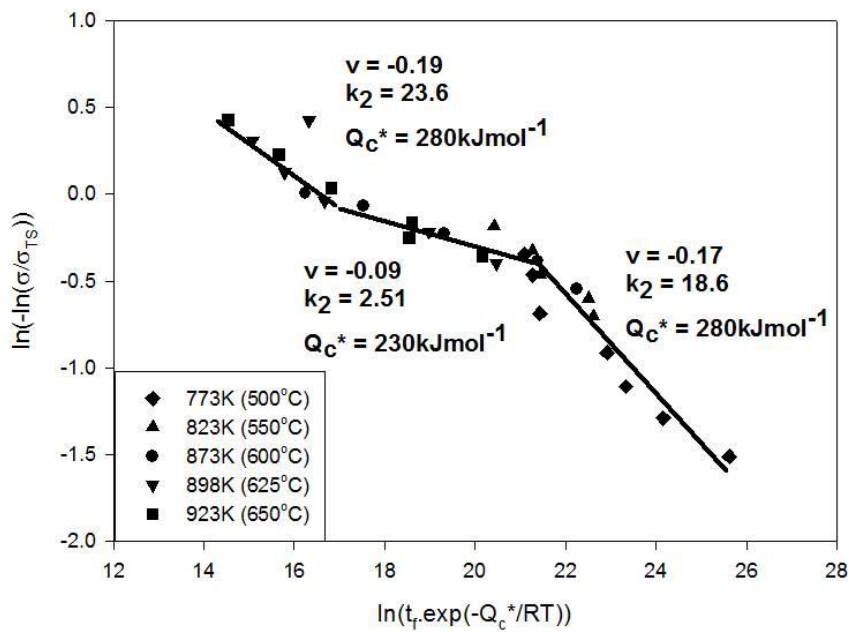

Figure 29: Adopting eqn.(2), plotting $\ln[\dot{\varepsilon}_m \cdot \exp(Q_c^*/RT)]$ as functions of $\ln[-\ln(\sigma/\sigma_{TS})]$, gives the k_2, v and Q_c^* figures listed in Table III for T23 steel.
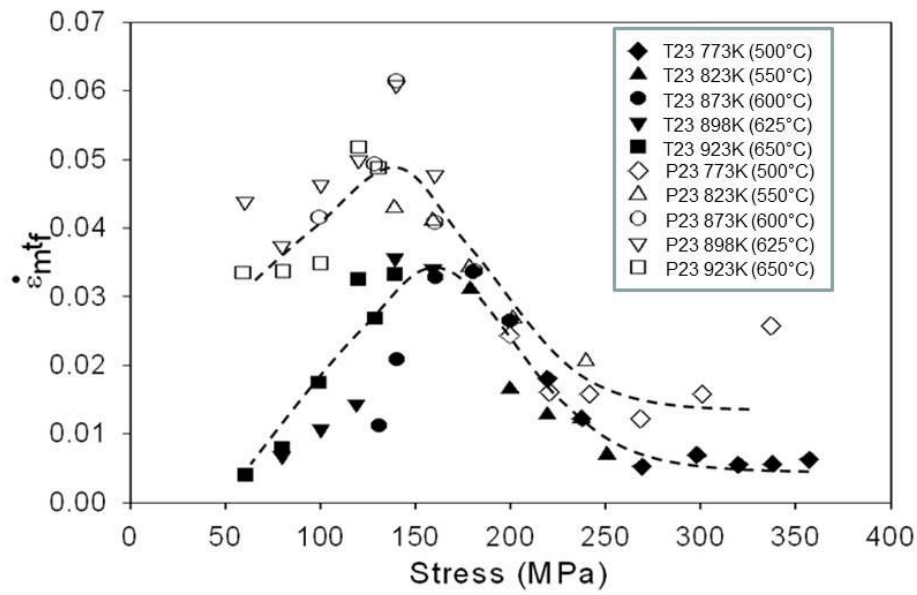
Figure 30: The stress dependence of $\dot{\varepsilon}_m t_f$ at 773-923K (500-650°C) for 2.25Cr-1.6W steel pipe (P23) and tube (T23).
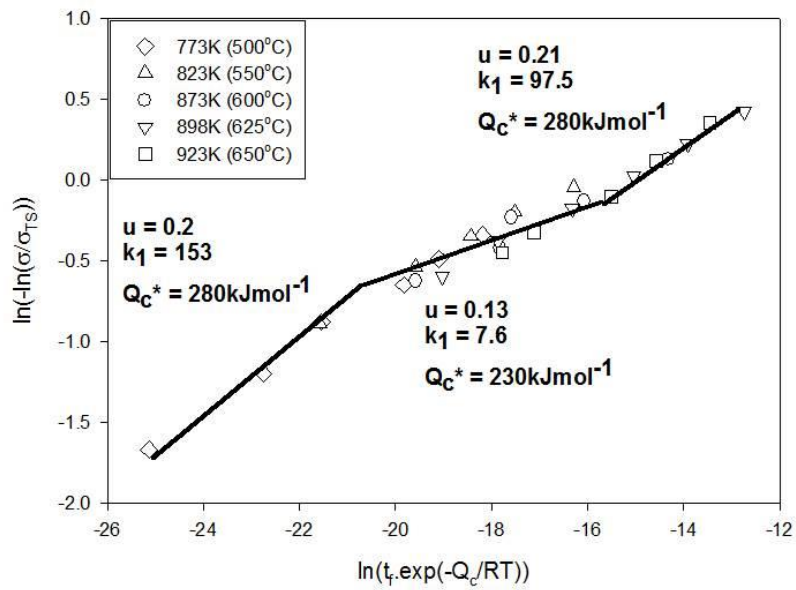
Figure 31: Adopting eqn. (1), plotting $\ln[t_f \cdot \exp(-Q_c*/RT)]$ against $\ln[-\ln(\sigma/\sigma_{TS})]$ gives the k_1, u and Q_c* figures listed in Table III for P23 steel.
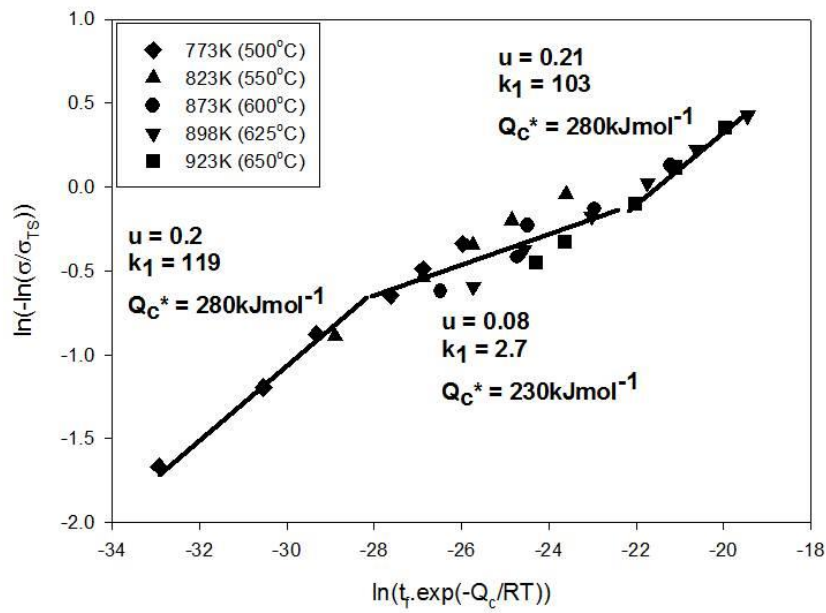
Figure 32: Adopting eqn. (1), plotting $\ln[t_f \cdot \exp(-Q_c^*/RT)]$ against $\ln[-\ln(\sigma/\sigma_{TS})]$ gives the k_1, u and Q_c^* figures listed in Table III for T23 steel.
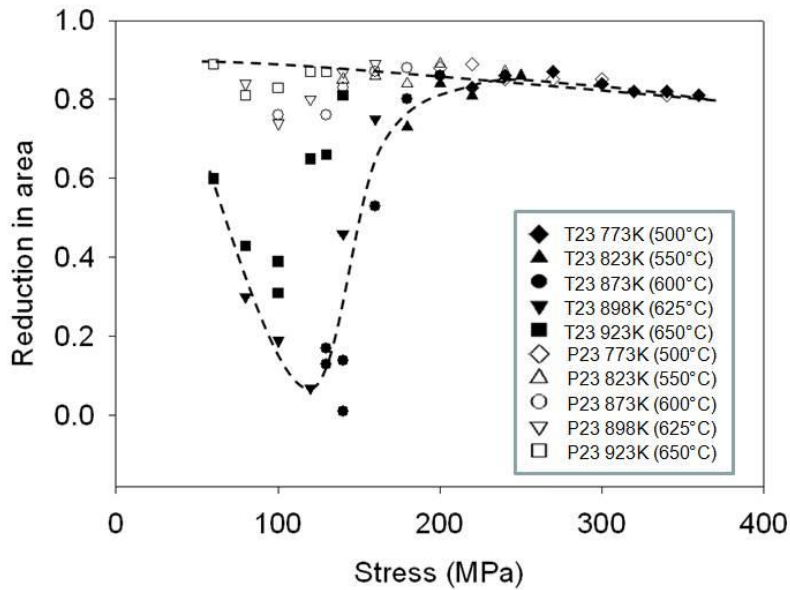
Figure 33: The stress dependencies of the reduction in area at fracture (RoA) at 773-923K (500-650°C) for 2.25Cr-1.6W steel pipe (P23) and tube (T23).
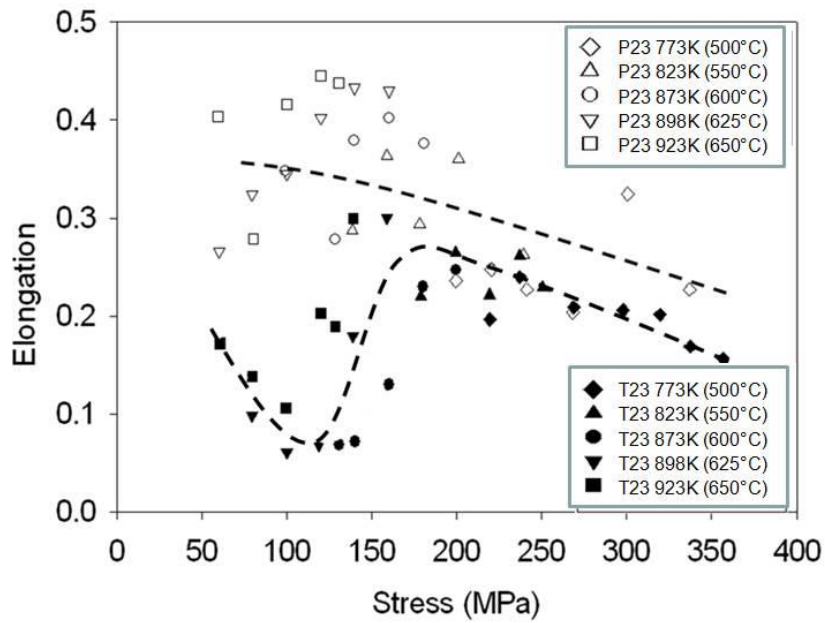
Figure 34: The stress dependencies of the total elongation at fracture (ε_f) at 773-923K for 2.25Cr-1.6W steel pipe (P23) and tube (T23).
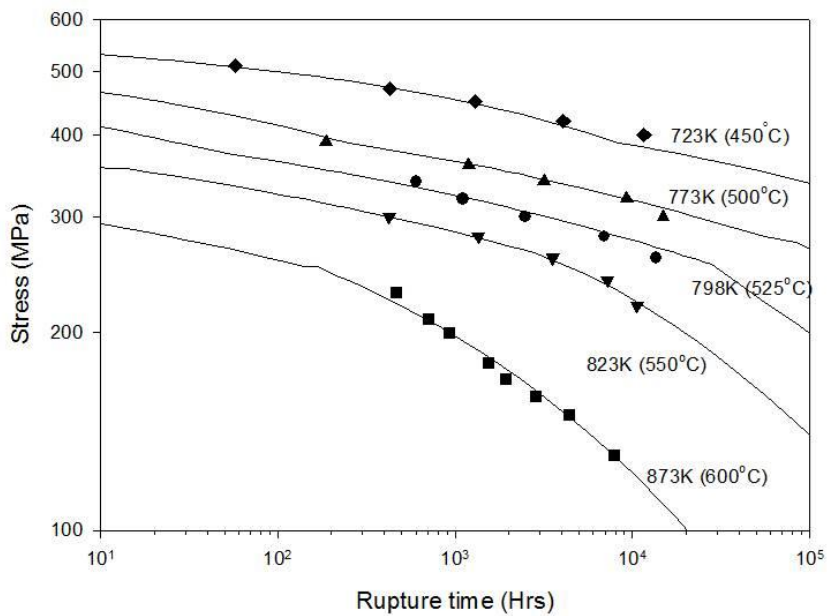
Figure 35: The stress dependence of the creep life of Gr.24 steel in the non-stress relieved condition, tested at 723 to 873K (450 to 600°C). The solid lines were predicted using eqn. (1) with the k_1, u and Q_c^* values for different (σ/σ_{TS}) ranges listed in Table V.
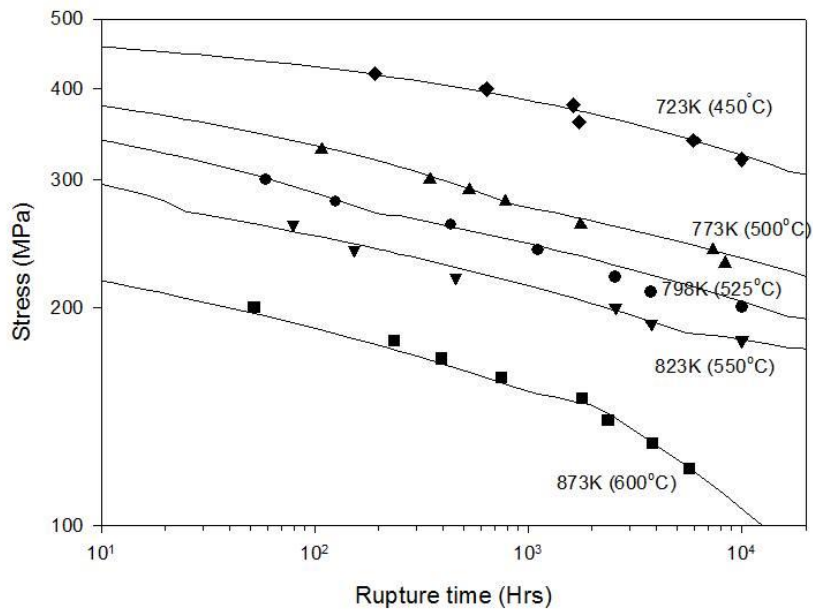
Figure 36: The stress dependence of the creep life of Gr.24 steel in the stress relieved condition, tested at 723 to 873K (450 to 600°C). The solid lines were predicted using eqn. (1) with the k_1, u and Q_c^* values for different (σ/σ_{TS}) ranges listed in Table V.
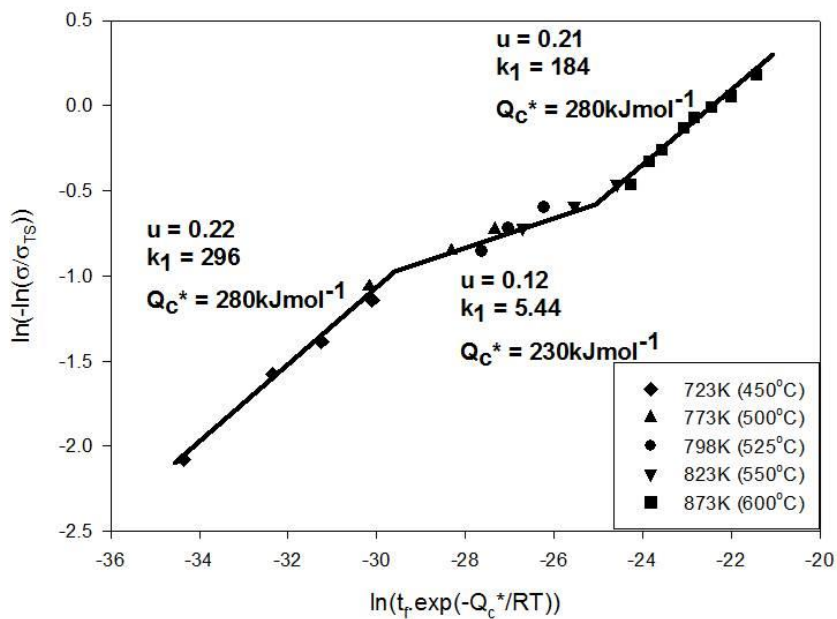

Figure 37: The variations of $\ln[t_f \cdot \exp(-Q_c^*/RT)]$ with $\ln[-\ln(\sigma/\sigma_{TS})]$ for Gr.24 steel in the non-stress relieved condition for tests carried out at 723 to 873K (450 to 600°C), giving the k_1, u and Q_c^* values for eqn.(1) listed in Table V.
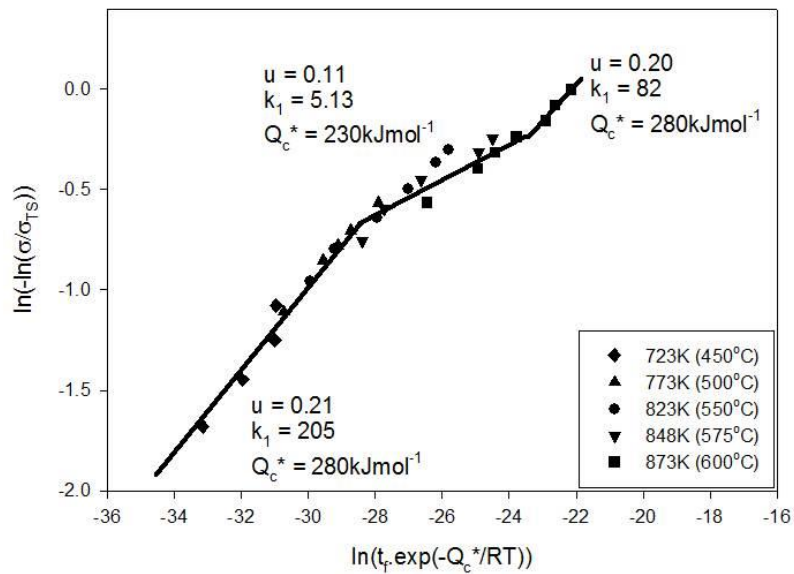
Figure 38: The variations of $\ln[t_f \cdot \exp(-Q_c^*/RT)]$ with $\ln[-\ln(\sigma/\sigma_{TS})]$ for Gr.24 steel in the stress relieved condition for tests carried out at 723 to 873K (450 to 600°C), giving the k_1, u and Q_c^* values for eqn.(1) listed in Table V.
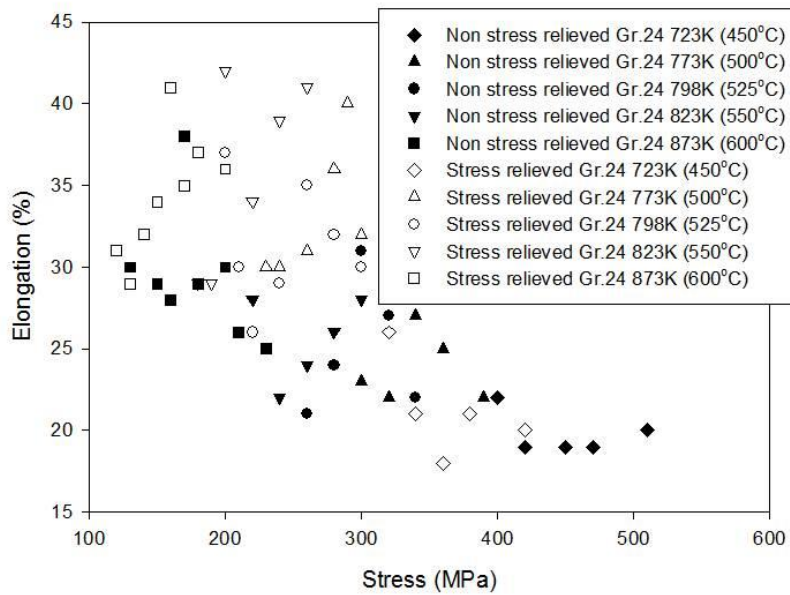

Figure 39: The variations of the reduction in area (closed symbols) and total elongation at fracture (open symbols) with stress and temperature for Gr.24 steels in the non-stress relieved condition tested at 723 to 873K (450 to 600°C).
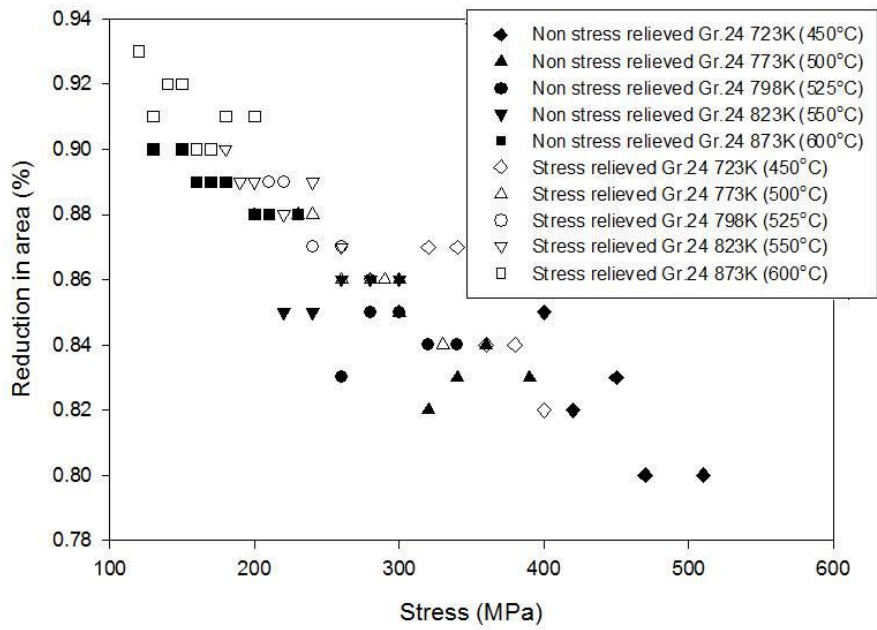
Figure 40: The variations of the reduction in area (closed symbols) and total elongation at fracture (open symbols) with stress and temperature for Gr.24 steels in the stress relieved condition tested at 723 to 873K (450 to 600°C).